JJ

BA-94-01

SW 9419

SIBYLL: An Event Generator for Simulation of High Energy Cosmic Ray Cascades

T.K. Gaisser and T. Stanev[1]
R.S. Fletcher[1,2]
Paolo Lipari[3]

Bartol Research Institute

SIBYLL: An event generator for simulation of high energy cosmic ray cascades

R.S. Fletcher[a,c] T.K. Gaisser[a] Paolo Lipari[b]
Todor Stanev[a]
[a]Bartol Research Institute, University of Delaware
Newark DE 19716
[b]Dipartimento di Fisica, Unitersità di Roma
Piazzale Aldo Moro 2, Rome
[c]Dept. of Physics, University of Arizona, Tuscon AZ*

January 21, 1994

Abstract

We describe the physical basis and some applications of an efficient event generator designed for Monte Carlo simulations of atmospheric cascades at ultra-high energies. The event generator (SIBYLL) incorporates many features of the Lund programs, but emphasizes the fragmentation region and the production of minijets. Consistent treatment of hadron-hadron and hadron-nucleus interactions is emphasized. Examples of applications are the calculation of coincident muons observed in deep underground detectors and simulation of the longitudinal development of air shower components in the atmosphere.

1 Introduction.

Traditionally, event generators used in simulations of air showers have been relatively simple parameterizations of accelerator data, with extrapolation to cosmic ray energy based on a combination of simple physical models and guesswork. There is good reason for this situation: shower simulations require large amounts of CPU time, and the data itself tends to have relatively large uncertainties. With the advent of increasingly sophisticated air shower experiments, the need for a more detailed treatment of hadronic interactions becomes urgent.

One example of a detailed interaction model for use in calculation of cosmic rays cascades is the one used in the program HEMAS [1]. This event generator is based on the UA5 Monte Carlo

*Present address.

extended to nuclear targets. Treatment of the central region (pseudorapidity less than 5) in the energy region up to $\sqrt{s} \approx 1$ TeV is precise. The fragmentation region, and in particular the leading nucleon distribution, is normalized to data at much lower, fixed target energy (~ 20 GeV) and cannot be directly confirmed from the collider data, which sees only the central region. Similarly, extrapolation beyond $\sqrt{s} \sim 1$ TeV involves assumptions beyond the data, and is not based on a consistent physical model.

Our goal in this work is to construct an event generator based on an underlying physical model, of comparable scope and detail to those used for studies of accelerator data, but tailored to the needs of cosmic ray cascade calculations. The model should reproduce in as much detail as possible the observed features of hadronic interactions at accelerator energies, including interactions on nuclear targets. Cascade development is dominated by minimum bias events, and secondary particles influence the cascade in proportion to their energy. It follows that correct treatment of the fragmentation region, including diffraction dissociation, is crucial. As mentioned above, data on particle production in the fragmentation region with nuclear targets is limited to relatively low energies. We therefore wish to use a physical model which provides a basis for extrapolation into unmeasured regions of energy and phase space.

In addition, because one of the main goals of air shower experiments is to determine the elemental composition of the primary cosmic radiation above 100 TeV, where it is not at present accessible to direct observation, we need also to treat heavy ion collisions. At present, the interaction of heavy ions in the atmosphere is treated externally in the cascade calculation as described in Ref. [2]. SIBYLL is, however, constructed so that it can be extended in a straightforward way to include interactions between heavy ions.

The physical model we use to treat all processes self-consistently and to provide an extrapolation into unmeasured regions of energy and phase space, is the dual parton model (DPM) [3] with minijet production [4, 5] superimposed. Many of the features of the model are thus borrowed from the Lund Monte Carlo algorithms, [6] but with parameters tuned to reproduce the fragmentation region data as well as the central region. An important technical difference is that SIBYLL is designed to work efficiently in the cascade context. It is designed to be called with a random sequence of interaction energies and projectile and target identities, rather than repeatedly with the same energy and particle types.

Related physical assumptions have been used recently by Wang and Gyulassy [7] and by Werner [8] to treat high energy heavy ion collisions. Their emphasis is on search for a transition

to a phase of quark-gluon matter and hence on central nucleus-nucleus collisions. For cosmic ray cascades, treatment of peripheral collisions between nuclei is at least as important, and is emphasized in our work [2].

In §2 we describe how we implement the minijet model for hadron-nucleon collisions in the context of the DPM algorithms. In §3 we discuss the extension of the model to nuclei. After a description of our assumptions for hadron-nucleon and hadron-air cross sections in §4, we compare in §5 the output of the simulation with a variety of hadron-hadron and hadron-nucleus interaction data, including the data used to tune the parameters of the model. Comparisons with fixed target data emphasize the fragmentation region. Collider data extends to higher energy but data are confined to the central region. We illustrate the model in §6 and §7 with two problems of current interest in high energy cosmic ray physics: coincident multiple TeV muons and longitudinal development of giant air showers. The first involves interactions in the range $E_{\rm lab} \sim 100$ to 10000 TeV ($0.5 < \sqrt{s} < 5$ TeV) and the second $\sqrt{s} \sim 50$ TeV. For these tests, we use the same external cascade program as in HEMAS, changing only the event generator. In this way we can compare to corresponding results obtained with the interaction model in HEMAS. Use of two completely independent approaches to extrapolation of hadronic interaction physics to air shower energies gives some measure of the corresponding systematic uncertainties.

Our attempt to find a model which treats all aspects of minimum-bias hadronic interactions in nuclei consistently on the basis of simple physical ideas has been only partially successful. In the conclusion we therefore give a critical discussion of the strengths and weaknesses of the event generator we have developed, along with a list of points that need further work. We also summarize the main features of the results and their implications for interpretation of cosmic ray cascades.

2 The Model

Hadron–proton interactions at fixed target energies show several simple and important features:

- A logarithmic increase of the average charged multiplicity $\langle n_c \rangle$
- KNO scaling of the multiplicity distribution, that is significantly wider than a Poissonian.
- A rapidity plateau of approximately constant height.
- Feynman scaling of the longitudinal momentum distributions.

- An average p_T of secondary particles that is approximately independent of energy.

The data from the collider experiments show a more complicated picture:

- The charged multiplicity increases faster than $\propto \ln s$ ($\langle n_c \rangle \propto \ln^2 s$ or $\propto s^{0.13}$) [9].
- The height of the rapidity distribution in the central region increases approximately logarithmically with energy.
- KNO scaling of the multiplicity distributions is violated. The distributions becomes wider, with increasing importance of the tail of high multiplicity events.
- Average p_T increases with energy.
- There is a positive correlation between the average p_T of charged particles and the multiplicity of the events.
- There are high p_T jets.

The goal is to produce a full simulation of hadronic interactions that reproduces all these qualitative features of the data. The basic philosophy of our model can be described in the following terms.

[1] Build a model of "low energy" hadron–hadron interactions where low energy corresponds to $\sqrt{s} \simeq$ 10–20 GeV, or E_{lab} = 50–200 GeV. The modeling of cross sections in this energy range should exhibit Feynman scaling. In this region there is a large amount of detailed experimental information on pp, $\pi^{\pm}p$ and $K^{\pm}p$ interactions, so that it is possible to verify the model.

[2] Model the new phenomena of the collider as the onset of a 'hard' part in the cross section, or the production of pairs of 'minijets'. The production of jet pairs with transverse momenta large compared to Λ_{QCD}, but small compared to the p_T of jets normally reconstructed at colliders, is common, and affects the properties of minimum bias events. By using perturbative QCD to calculate the parton–parton cross sections for interactions with a scale of order 2 GeV it is possible to reproduce both the increase of the $p\overline{p}$ cross section and many of the qualitative features of differential cross sections described above.

[3] Finally we build a model to pass from hadron–hadron to hadron–nucleus interactions. At low energy data is available both for hadron–hadron and hadron–nucleus interactions. It is therefore possible again to test the model in this energy range.

2.1 Low energy interactions

2.1.1 Non-diffractive events

The central idea for the "low p_T" hadron–hadron events is to model these interactions as the production and subsequent fragmentation of two color strings [3]. Consider for example a proton–proton interaction. In such an event it is assumed that each nucleon is composed of a valence diquark (a color antitriplet) and a valence quark (color triplet). During the interaction, the hadrons exchange very soft gluons which reorganize the color field. The diquark from the projectile combines with the quark of the target and vice–versa. This leaves two color strings stretched between the remnants of the outgoing nucleons, which then fragment into hadrons.

The energy of each proton is split between the quark and the diquark. The fractional energy x_q of the quark fragment is chosen according to

$$f_q(x) = \frac{(1-x)^\alpha}{[x^2 + \mu^2/s]^{1/4}} \tag{1}$$

where $\mu = 0.35\ GeV$ acts as an 'effective quark mass' We choose $\alpha = 3.0$ both for a quark opposite a ud diquark and for a quark opposite a uu diquark in the proton. Each string has energy $E_{str} = \frac{\sqrt{s}}{2}(x_1 + x_2)$ and longitudinal momentum $p_{str} = \frac{\sqrt{s}}{2}(x_1 - x_2)$, where x_1 is the fractional energy of the (di)quark at the "projectile end" of the string, and x_2 is the fractional energy of the (di)quark at the "target end" of the same string. The generalization to the case of meson–nucleon interaction is obvious. In this case the meson is excited into a valence quark–antiquark pair, that combine with the valence diquark and the valence quark to produce two colorless strings that are then fragmented.

Each string is fragmented in its own center of mass system (where it has a mass $E^*_{str} = \sqrt{sx_1x_2}$) according to fragmentation algorithms very similar to the standard Lund algorithms [10]. The string (in its own c.m. reference frame) is fully described by the flavor of the (anti) quarks and/or (anti) diquarks at its ends and by its total energy. To produce a particle, one end of the string is chosen at random. A new q–$\overline{q}$ (or $\overline{qq}$–qq with relative probability $P_{qq}/P_q = 0.04$) is produced, and the new flavor combines with the flavor at the chosen end of the string to

produce a hadron. In the case of of q–$\overline{q}$ pairs the production of strange quarks is suppressed: $P_s/P_{d,u} = 0.25$. A meson state of a given flavor will have spin 1 or spin 0 with relative probability $P_V/P_S = 0.3$. The states $u\overline{u}$, $d\overline{d}$, $s\overline{s}$ give raise to the mesons (π°,η, η') or (ρ°,ω,ϕ) according to the usual flavor content of the different mesons.

The treatment of the diquarks states follows very closely the work of the Lund group. Diquarks are characterized by their flavor and their spin. Diquark states composed of identical quarks (uu, dd and ss) can only have spin 1, the other states can have spin 0, or 1. Taking into account isospin symmetry there are 5 different probabilities: $P_{(ud)_0}$, $P_{(ud)_1,(uu)_1,(dd)_1}$, $P_{(us)_0,(ds)_0}$, $P_{(us)_1,(ds)_1}$, $P_{(ss)_1}$. These probabilities are calculated according to $P_{(us)}/P_{(ud)} = P_{(ss)}/P_{(us)} = 0.075$ and $P_{(ud)_1}/P_{(ud)_0} = P_{(us)_1}/P_{(ud)_0} = 0.42$. All the baryons of the spin $\frac{1}{2}$ octet and the spin $\frac{3}{2}$ decuplet can be constructed combining quarks and diquarks, and taking into account the spin–flavor content of different baryons according to the SU(6) group. The probability of the decuplet is suppressed with respect to the octet by an additional factor $P_{\frac{3}{2}}/P_{\frac{1}{2}} = 0.15$.

By default, all pions, kaons and nucleons are treated as stable particles by the event generator, with their decays (where relevant) to be dealt with in the cascade program. Decay of resonances occurs inside the event generator.

Whenever a $q\bar{q}$ pair (or diquark) is created during string fragmentation, some transverse momentum is produced. This p_T is generated from a Gaussian distribution such that

$$\langle p_T \rangle = p_0 + 0.184 \ln\left(\frac{\sqrt{s}}{30 \text{ GeV}}\right) \tag{2}$$

where $p_0 = 0.3$ GeV for u, d quarks, 0.45 GeV for s-quarks and 0.6 GeV for diquarks. Equal and opposite p_T's are given to the quark (di-quark) in the produced particle, and to the newly produced quark (di-quark) attached to the end of the remaining string. Thus, for example, the transverse momentum of a meson is the vector sum of its two constituent quark momenta.

The energy of each produced particle is generated according to the Lund fragmentation function [10],

$$f(z) = \frac{(1-z)^a}{z} \times \exp\left(\frac{-b\ m_T^2}{z}\right) \tag{3}$$

where z is the fractional energy of the produced hadron relative to its parent quark or di-quark and $m_T^2 = \sqrt{p_T^2 + m^2}$. To fit to particle production in low energy hadronic interactions we use $a = 0.5$ and $b = 0.8$. This fragmentation algorithm would generate a leading proton spectrum significantly softer than found at fixed target experiments. Because of the importance of the

compared to HQCD, but minor compared to the p_T of jets normally reconstructed at colliders, is common, and affects the properties of minimum bias events. By using perturbative QCD to calculate the parton–parton cross sections for interactions with a scale of order 2 GeV it is possible to reproduce both the increase of the $p\bar{p}$ cross section and many of the qualitative

leading particles to cosmic ray shower development, we use a special, harder fragmentation function to generate the energy of the baryon containing the original diquark from the beam or target nucleons. Once a new particle is generated, we are left with a new, shorter (i.e. lower energy) piece of string and a newly produced quark at one end, and the algorithm starts again.

This algorithm repeatedly splits "string $\rightarrow$ particle+string". When the string energy becomes too small the algorithm breaks down. To finish the fragmentation, a separate procedure is needed which will produce two final hadrons and exactly conserve energy and momentum. When, after a quark flavor is chosen, the remaining string mass is less than a threshold value, $M_{\rm th}$ two final hadrons are produced. A p_T is chosen in the usual way from Eq. 2. The threshold mass is 1.1 ± 0.2 GeV greater than the sum of the quark masses that comprise the final two hadrons. As in two body scattering, the total energy, the particle masses and the p_T completely determine the kinematics of the 2 final particles. Finally, all particles are boosted from the string rest frame to the center of mass frame.

2.1.2 Diffractive events

The algorithm described so far gives a good description of non-diffractive interactions, but does not include diffractive dissociation. Because of the different kinematic structure of diffractive events, they can be important to the study of air showers [11]. We have therefore included the following phenomenological description of diffractive events in SIBYLL [12].

The diffractive cross section can be divided into three parts, forward (beam) diffraction, backward (target) diffraction, and double (beam and target) diffraction. We parameterize the diffractive cross sections with a simple logarithmic function. The forward and backward diffractive cross sections are each chosen to be 9% of the inelastic cross section at 30 GeV or about 3. mb at low energies. The double diffractive cross section is 4% of the inelastic cross section. A logarithmic term is added to fit the rise of the diffractive cross sections. These cross sections are compared to measurements of the single diffractive cross sections in Figure 1.

In a diffractive event one or both of the incoming particles is excited to a high mass state, X. The excited state then decays to a group of particles. The mass of the excited state is generated according to a distribution $\propto M_X^{-2}$ with the limits: $M_X^2[\min] = 1.5$ GeV^2 for excitation of a nucleon or antinucleon, 0.2 GeV^2 for excitation of a $\pi^{\pm}$, and 0.6 GeV^2 for

excitation of a kaon. The maximum value of the mass is chosen according to the coherence condition $M_X^2[\max] = 0.1\ s$. [14, 15] The sharp cutoff is artificial, but the relative normalization of 'low masses' and 'high masses' is correct. In the case of excitation of π's and K's we have chosen $M_X[\min] \approx m_h + m_\pi + 0.150\ GeV$ which reproduces the result for pp. The momentum transfer t is generated according to an exponential distribution

$$\frac{d\sigma_{diff}}{d|t|} \propto \exp[-b(M_X^2)|t|], \tag{4}$$

with $B(M_X^2) = 6.5\ \mathrm{GeV}^{-2}$ for $M_X^2 > 5\ \mathrm{GeV}^2$ and increasing logarithmically for smaller values of excited mass.

We use two algorithms for decay of the excited state, depending on its mass. For $(M_X - m_h) \leq 0.6\ GeV$ the decay is determined by the phase space for $X \rightarrow h' + n\pi$'s, where h' is h or a hadron related to h by isospin, (*e.g.* if h is a proton then h' can be a proton or a neutron, with relative probability 2:1). The distribution of the number of π's produced is a gaussian with $\langle n_\pi \rangle = 2\sqrt{M_X - m_h}$ (in GeV) and $\sigma_{n_\pi}^2 = \frac{1}{2}\langle n_\pi \rangle$.

As noted in Ref. [1], data on diffractive excitation at high energy [16] are inconsistent with isotropic decay of the excited mass. Therefore, for larger masses, the decay of the excited state is modeled by splitting it into two valence components (quark–antiquark in the case of an excited meson and quark–diquark in the case of an excited baryon), and stretching a string of mass M_X between the two partons. The string is fragmented as usual. The string carries the momentum of the excited particle X, and the ends of the string move along the momentum axis of the particle, *i.e.* no additional p_T is created at the 'ends' of the strings. The orientation of a baryonic string is chosen so that the diquark from the interacting beam is at the forward end of the string.

This algorithm reproduces the basic features of the low energy cross sections described at the beginning of this section. To extend the model to high energies we need to include minijet production.

2.2 The Minijet model.

There is ample experimental evidence that production of small (several GeV) jets becomes important as the interaction energy increases. At 540 GeV, for example, the UA1 Collaboration[17] finds that events containing jets with transverse momenta of 5 GeV or more make up one third of the cross section. In the minijet model, [4, 5] perturbative QCD is extended to even lower momentum scales. Such very soft jets cannot be reconstructed by standard jet finding algorithms,

but they affect the properties of the minimum bias event sample. In particular, they contribute to the rise of average p_T with center of mass energy, to the rise of the central rapidity density and total multiplicity and to the observed correlation between $\langle p_T \rangle$ and multiplicity. The basic formulas for our Monte Carlo treatment of minijet production were described in Ref. [18]. We summarize them here for completeness.

An underlying assumption and constraint on the model is that minijet production is related to the rise in hadronic inelastic cross section [19]. The physical picture is that a parton from the beam hadron (h_1) makes a "hard" collision with a parton in the target hadron (h_2). The cross section for hard interactions is described in perturbative QCD by

$$\sigma_{QCD}^{(h_1 h_2)}(\sqrt{s}) = \int dx_1 \int dx_2 \int_{Q^2_{\rm min}}^{Q^2_{\rm max}} d\hat{t} \, \frac{d\sigma_{QCD}^{(h_1 h_2)}}{dx_1 dx_2 dQ^2}(x_1, x_2, Q^2; \sqrt{s}), \tag{5}$$

where the integration region satisfies the constraint

$$\hat{s} = x_1 x_2 s = |\hat{u}| + |\hat{t}| > 2\, Q^2_{\rm min}. \tag{6}$$

The integrand in Eq. 5 is

$$\frac{d\sigma_{QCD}^{(h_1 h_2)}}{dx_1 dx_2 dQ^2} = \sum_{i,j} \frac{[f_i^{h_1}(x_1) f_j^{h_2}(x_2) \hat{\sigma}_{ij}(\hat{s}, \hat{t}, \hat{u}) + f_j^{h_1}(x_1) f_i^{h_2}(x_2) \hat{\sigma}_{ij}(\hat{s}, \hat{u}, \hat{t})]}{1 + \delta_{ij}}, \tag{7}$$

where the sum is over all parton types and $f_i^h(x)$ is parton distribution function for parton type i in hadron h. The $\hat{\sigma}_{ij}(\hat{s}, \hat{t}, \hat{u})$ are elementary differential cross sections $d\hat{\sigma}/d\hat{t}$ for the different QCD processes. The lower limit on the integral in Eq. 5 must be taken large enough so that the perturbative calculation of the cross sections is valid. We choose $Q^2_{\rm min} = 5$ GeV^2 and multiply the jet cross section by an *ad hoc* k-factor of 1.7 to fit both the cross section and the mean multiplicity at high energy.

The QCD cross section (5) has been calculated separately and is included in the SIBYLL program in tabular form. We have used $\alpha_s = \frac{12\pi}{(33-2N_{\rm flav})\ln(Q^2/\Lambda^2)}$ with $N_{\rm flav} = 4$ for $Q^2 \leq 25$ GeV^2. We use the EHLQ[20] parameterization of the proton structure functions, and correspondingly choose $\Lambda_{QCD} = 0.20$ GeV. At very small momentum fraction x the EHLQ parameterization does not apply. Below $x = 10^{-4}$ we extrapolate using the ansatz of Gribov, Levin & Ryskin [21], but we have not included any saturation effects due to shadowing of partons by each other [21].

For Q^2_{min} of several GeV^2, this jet cross section rises quickly and becomes larger than the total cross section, as shown in Fig. 1. This can be understood [5] as follows. Equation 5 is the total inclusive cross section for jet production, which is larger than the total inelastic cross section when the average multiplicity of hard interactions is greater than one. Thus, as suggested by Durand & Pi, [5] we take the average number of hard interactions at impact parameter b of the hadron-hadron system as

$$n(b,s) = A(b)\,\sigma_{\rm QCD}(s), \tag{8}$$

where $A(b)$ represents the probability for a collision between partons in the colliding hadrons. If $\rho(b)$, the distribution in impact parameter space of partons in an incident nucleon, is taken to be the Fourier transform of the proton electric form factor then

$$\begin{aligned} A_{pp}(b) &= \int \mathrm{d}^2b'\rho(|\mathbf{b}-\mathbf{b}'|)\rho(b') \\ &= \frac{\nu_p^2}{12\pi}\,\frac{(\nu_p b)^3}{8}\,K_3(\nu_p b), \end{aligned} \tag{9}$$

with $\nu_p^2 = 0.71$ GeV^2. The normalization is such that $\int A(b)\mathrm{d}^2b = 1$.

For $\pi - p$ interactions we apply the same model. For the parton density on the pion side we use a monopole form factor, so that

$$A_{\pi p}(b) = \frac{\nu_p^2}{2\pi}\frac{1}{(1-\zeta)}\left[\frac{\nu_p b}{2}\,K_1(\nu_p b) + \frac{\zeta}{(1-\zeta)}\,[K_0(\nu_\pi b) - K_0(\nu_p b)]\right] \tag{10}$$

where $\zeta = (\nu_p/\nu_\pi)^2$ and $\nu_\pi^2 = 0.54$ GeV^2. For pions we use the parameterization of the structure functions from Ref. [22].

When the expression (8) is included into the eikonal model for hadron-hadron scattering [23, 24], one has a complete model for the scattering process, which, in principle, should fit data on total cross section, elastic slope parameter B and the ratio of real to imaginary part of the scattering amplitude. The elastic scattering amplitude is

$$f(s,q) = \frac{ik}{2\pi}\int \mathrm{d}^2b\, e^{i\vec{q}\cdot\vec{b}}\left[1 - e^{-\chi(b,s)}\right], \tag{11}$$

and the corresponding expression for the inelastic cross section (assuming a real eikonal function) is

$$\sigma_{\rm inel} = \int \mathrm{d}^2b\left[1 - e^{-2\chi(b,s)}\right]. \tag{12}$$

The complete eikonal is [5]

$$\chi(b,s) \;=\; \chi_{\rm hard}(b,s) \,+\, \chi_{\rm soft}(b,s), \tag{13}$$

where $\chi_{\rm hard} = \frac{1}{2}n(b,s)$. The hard part of the eikonal has the simple interpretation that $\exp\{-n(b,s)\}$ is the probability that there are no minijets produced in a collision at impact parameter b.

The soft part of the eikonal function is assumed to be related to the shape of the hadrons as measured by their electric form factors [23, 24]. Following the original simple *ansatz* of Ref. [5], we take $\chi_{\rm soft}(b,s) = 2\,C\,A(b)$ with C independent of energy and the profile function $A(b)$ as given in Eqs. 10 and 10. The choice $C = 123$ GeV^{-2} reproduces the low energy inelastic cross section of 32 mb.

In order to fit the eikonalized minijet model to data on elastic and total cross sections, it is necessary to allow for the possibility that the gluons have a broader distribution (by about 20%) than the valence quarks [25, 26]. The valence quark distribution is assumed to be determined by the electric form factor, and the gluons are assumed to be distributed around the valence quarks, with a distribution characterized by a monopole form factor, which introduces a second parameter. Lipari [27] discusses in detail the fits to elastic scattering and total cross section that can be obtained in this way. This type of model leads to a different form for the profile function for hard scattering. For simplicity here, however, we use the same profile function, determined by the electric form factors, for both hard and soft scattering. The resulting proton-proton and pion-proton cross sections are compared to data [28, 29] in Fig. 1.

We can rewrite Eq. 12 as

$$\sigma_{\rm inel} = \sum_{N=1}^{\infty} \sigma_N + \int e^{-n(b,s)}[1 - e^{-2\,C\,A(b)}]{\rm d}^2b, \tag{14}$$

where

$$\sigma_N = \int \frac{[n(b,s)]^N}{N!}\, e^{-n(b,s)}\, {\rm d}^2b. \tag{15}$$

2.2.1 Production of minijets

Equation 15 is the basis of the Monte-Carlo implementation of the minijet model [18]. We interpret σ_N as the topological cross section for production of N pairs of mini-jets (N hard interactions). This interpretation follows from the AKG cutting rules [21]. The quantity σ_N is

the term in the AKG expansion with exactly N cut ladders exchanged, summed over all uncut ladders. The probability distribution for minijet production is

$$P_N = \frac{\sigma_N}{\sigma_{inel}}, \tag{16}$$

and the mean number of minijet pairs per interaction is

$$\langle N \rangle = \sum_{N=0}^{\infty} N P_N = \frac{\sigma_{\rm QCD}(s)}{\sigma_{\rm inel}}. \tag{17}$$

To generate an inelastic, non-diffractive event, we start by choosing randomly the number of minijet pairs to be produced.The values of x_1 and x_2 are chosen from the parton distributions in the incident hadrons subject to the constraint 6. In selecting x_1 and x_2 we use the approximation of a single distribution function for all partons,

$$f(x) = g(x) + \frac{4}{9}\,(q(x) + \bar{q}(x))$$

without scaling violations. Similarly, in choosing the transverse momentum of the jet pair, we use a single differential cross section,

$$\frac{d\hat{\sigma}}{d\hat{t}} \propto \frac{1}{\hat{t}^2},$$

with $\hat{t} > Q^2_{\rm min}$. We emphasize, however, that in calculating the $N_{\rm jet}$ distribution from 16 we have treated the various combinations of parton-parton scattering separately as shown in Eqs. 5, 7 and we have used properly evolved structure functions.

Each pair of jets is represented as a loop of string stretched between gluons [6]. This loop is not connected to the strings constituting the underlying event. Because of the loop topology, gluon fragmentation is slightly different from fragmentation of strings in the underlying event. First a leading particle is created at each end of the loop by generating two $q\bar{q}$ pairs at each end. The remaining two strings are then fragmented normally. This gives a minimum of 6 particles per jet pair.

2.2.2 Diffraction dissociation at high energy

Diffraction dissociation is not included in the minijet model. Because diffractive events contain no minijets, they should in principle be included in the cross section for zero jets. Indeed, the constant C in Eq. 14 is chosen so that at low energy $\sigma_{\rm inel}$ includes diffraction dissociation. In

the formalism described above, however, the expression (14) gives for the inelastic cross section for no jets,

$$\sigma_{\rm nojet} = \int e^{-n(b,s)}[1 - e^{-2\,C\,A(b)}]{\rm d}^2b. \tag{18}$$

In the low energy limit, $\sigma_{\rm nojet} \to 32$ mb; however, it vanishes at high energy as a consequence of the increase in $\sigma_{\rm QCD}$. Although it is possible that diffractive dissociation vanishes at high energy, present data (as well as theoretical expectation) are more suggestive of a logarithmic increase in diffractive dissociation, as described in §2.1.2 [15].

What we have done instead is simply to force diffractive dissociation with the probability

$$P_{\rm diff} = \frac{\sigma_{\rm diff}}{\sigma_{\rm inel}}. \tag{19}$$

For each event, the first random decision is whether the event is diffractive. If not, then Eq. 14 is used to determine how many minijets are produced or whether the event is a non-diffractive inelastic event with no jets. For example, the probability of producing N minijet pairs is $P'_N = (1 - P_{\rm diff})\,\sigma_N/\sigma_{\rm inel}$ instead of P_N from Eq. 16. To the extent that diffraction is not included in the calculation of $\sigma_{\rm inel}$, this is inconsistent in principle. We believe, however, that in practice the effects on cascades of diffraction as well as of minijet production will be represented as we intend. Moreover, with this structure it is possible to explore the effects of different assumptions about extrapolation of diffraction to high energy in a straightforward way.

3 Hadron–nucleus cross sections

3.1 Hadron–nucleon interaction parameters

The hadron–nucleus and nucleus–nucleus cross sections are determined from the basic parameters of hadron–nucleon scattering. For a given value of $\sqrt{s}$ these are $\sigma_{\rm tot}$, the elastic slope parameter B and the ratio of the real to the imaginary part of the forward scattering amplitude ρ. In our shower code the hadron–nucleus and nucleus–nucleus cross sections are internally consistent with each other because are calculated [2] from the same hadron–nucleon input. Since the minijet model in its eikonal form is a model for the hadron–nucleon scattering amplitude, we could in principle use B and ρ from that model as input for the cross sections. We have chosen not to enforce the model this rigidly, however. Although we use the minijet model results (14) for the hadron–nucleon inelastic cross section, we have kept B and ρ as separate inputs and used the parameterization of Block & Cahn [28] for them.

We use the standard approximation [28] for the two-body elastic scattering amplitude

$$f(q) \simeq \frac{k\,\sigma_{\rm tot}}{4\pi}(i+\rho)\,e^{-Bq^2/2}. \tag{20}$$

The hadron–nucleon profile function $\Gamma(b)$ is the Fourier transform of the elastic scattering amplitude

$$\Gamma(b) = \frac{1}{2\pi\,ik}\int \mathrm{d}^2q\,e^{-i\mathbf{q}\cdot\mathbf{b}}f(q) \simeq \frac{\sigma_{\rm tot}\,(1-i\rho)}{4\pi B}\exp\left\{-\frac{b^2}{2B}\right\}. \tag{21}$$

The hadron–nucleon cross sections can be written in terms of the profile function. The optical theorem for the total cross section $\sigma_{\rm tot} = 4\pi/k\ \Im[f(0)]$, and the definition of the differential elastic scattering cross section as $d\sigma/d\Omega = |f(q)|^2$ lead to the result

$$\sigma_{\rm inel} = \sigma_{\rm tot} - \sigma_{\rm el} = \int P(b)\,\mathrm{d}^2b, \tag{22}$$

where

$$P(b) = 1 - |1-\Gamma(b)|^2. \tag{23}$$

The relation (22) leads to the interpretation of $P(b)$ as the probability of an inelastic interaction between the projectile hadron and a single nucleon at impact parameter b.

3.2 Total, Elastic and Quasi–elastic cross sections

In Glauber scattering theory [30] the amplitude for the scattering $hA \to hA^*$ from an initial nuclear state $|i\rangle$ (the ground state) to a final state $|f\rangle$ without pion production and with transfer momentum q is

$$F_{if}(q) = \frac{ik}{2\pi}\int \mathrm{d}^2b\ e^{i\mathbf{q}\cdot\mathbf{b}}\ \Gamma^{hA}_{if}(b) \tag{24}$$

where

$$\begin{aligned}\Gamma^{hA}_{if}(b) &= \langle f|\left\{1-\prod_{j=1}^{A}[1-\Gamma(\mathbf{b}-\mathbf{r}_{\perp j})]\right\}|i\rangle \qquad (25)\\ &\equiv \int\prod_{k=1}^{A}\mathrm{d}^3r_k\ \Psi_f^*(\mathbf{r}_1,\ldots,\mathbf{r}_A)\left\{1-\prod_{j=1}^{A}[1-\Gamma(\mathbf{b}-\mathbf{r}_{\perp j})]\right\}\Psi_i(\mathbf{r}_1,\ldots,\mathbf{r}_A)\end{aligned}$$

From these expressions it is possible to derive [31] the formulas we use for the various hadron–nucleus cross sections. The total cross section is:

$$\begin{aligned}\sigma^{hA}_{\rm tot} &= \frac{4\pi}{k}\,\Im\{F_{ii}(0)\}\\ &= 2\int \mathrm{d}^2b\int\prod_{k=1}^{A}\mathrm{d}^3r_k\ \rho_k(r_k)\ \Re\left\{1-\prod_{j=1}^{A}[1-\Gamma(\mathbf{b}-\mathbf{r}_{\perp j})]\right\} \qquad (26)\end{aligned}$$

where we have used the approximation $|\Psi_i(\mathbf{r}_1,\ldots,\mathbf{r}_A)|^2 \simeq \sum_{k=1}^{A} \rho_k(r_k)$, and $\rho_k(r)$ is the density distribution of the k–th nucleon in the nucleus with the normalization $\int \mathrm{d}^3r\, \rho_k(r) = 1$. For atmospheric nuclei we use densities given by shell-model wave functions, [32] as discussed in Ref. [2], with $\sqrt{\langle r^2\rangle} = 2.54$ fm for nitrogen and 2.718 fm for oxygen. Note that in the shell model nucleons belonging to different shells have different spatial distributions, and that is why we do not take the densities $\rho_k(r)$ as all identical. The elastic cross section can be obtained as:

$$\begin{aligned}\sigma_{\rm el}^{hA} &= \int \mathrm{d}^2b\, |\Gamma_{ii}^{hA}(b)|^2 \\ &= \int \mathrm{d}^2b \left| \int \prod_{k=1}^{A} \mathrm{d}^3r_k\, \rho_k(r_k) \left\{ 1 - \prod_{j=1}^{A} [1 - \Gamma(\mathbf{b} - \mathbf{r}_{\perp j})] \right\} \right|^2 \end{aligned} \tag{27}$$

The sum of the elastic and quasielastic (when the target nucleus is excited or fragmented without production of new particles) cross section is

$$\begin{aligned}\sigma_{\rm qe}^{hA} + \sigma_{\rm el}^{hA} &= \sum_f \int \mathrm{d}^2b\, |\Gamma_{if}^{hA}(b)|^2 \\ &= \int \mathrm{d}^2b \int \prod_{k=1}^{A} \mathrm{d}^3r_k\, \rho_k(r_k) \left| \left\{ 1 - \prod_{j=1}^{A} [1 - \Gamma(\mathbf{b} - \mathbf{r}_{\perp j})] \right\} \right|^2 \end{aligned} \tag{28}$$

where we have used the completeness relation $\sum_f |f\rangle\langle f| = I$.

Typically in calculation of air showers, elastic as well as quasi–elastic scattering are omitted both from the interaction model and from the cross sections used to obtain the interaction lengths in air. The omission of these processes is justified on the grounds that no secondary particles are produced and the projectile loses no energy. In principle, however, they should be included since they contribute to the deflection of particles from the direction of the incident primary and hence to the lateral distribution of shower particles.

To include these processes, we use the total hadron–nucleus cross sections to determine the interaction lengths, and the first step when a particle interacts is then to decide whether an elastic or quasi–elastic interaction is to occur, according to the values of $\sigma_{\rm el}^{hA}$ and $\sigma_{\rm qe}^{hA}$ relative to $\sigma_{\rm tot}^{hA}$ calculated as above. In elastic or quasi–elastic processes the transverse momentum of the scattered projectile particle is generated from an exponential distribution $\propto \exp[-B_{eff}^{\rm el,qe} p_T^2]$, the direction of the particle is recalculated, and the procedure returns to the next event in the cascade. Otherwise an inelastic hadron–nucleus event is generated. In case of elastic scattering the exact shape of the differential distribution can be easily calculated from the amplitude

(24), it is however a good approximation to simply use an effective slope $B^{\rm el}_{eff} \simeq B + \frac{1}{3}a^2$, where B is the slope for hadron–nucleon elastic scattering and a^2 is the mean square radius of the target nucleus. In the case of quasi–elastic scattering the effective slope depends on the number of target nucleons that are participating in the scattering[31]: $B^{\rm qe}_{eff} \simeq B/\sqrt{n}$. Using a Gaussian approximation for the nuclear density as well as for the elastic hadron–nucleon scattering amplitude, the expansion of the quasi elastic cross section in terms of the number of participating nucleons n can be written [33] as:

$$\sigma^{hA}_{\rm qe} \;=\; \frac{2}{3}\pi\langle r\rangle^2 \sum_{n=1}^{A} \frac{\epsilon^n}{n}, \tag{29}$$

where

$$\epsilon \;=\; \frac{\sigma^{\rm tot}_{pp}}{B}\,\frac{1+\rho^2}{16\pi}. \tag{30}$$

We have used this approximate expression to compute the relative contribution of the n–th multiple scattering term to quasi–elastic scattering, but we have used the full shell–model density expressions in the calculation of $\sigma^{hA}_{\rm qe}$. The various components of the hadron-air cross sections are shown in Fig. 2.

3. Wounded nucleon distribution

The cross section for hadron–nucleus scattering with the production of pions is

$$\sigma^{hA}_{\rm prod} \;=\; \sigma^{hA}_{\rm tot} - \sigma^{hA}_{\rm el} - \sigma^{hA}_{\rm qe} = \int {\rm d}^2b\,\left\{1 - \prod_{j=1}^{A}[1 - P^{hA}_j(b)]\right\}, \tag{31}$$

where

$$P^{hA}_j(b) = \int {\rm d}^3r\;\rho_j(r)\;P(|{\rm b} - {\rm r}_\perp|) \tag{32}$$

and the function $P(b)$ is given in equation (23). The expression (31) can have a simple interpretation, in terms of a naive scattering picture, in a collision at impact parameter b, the incident hadron has probability P_j of interacting (with pion production) with the j–th nucleon in the target nucleus, and therefore the probability of at least one interaction in the collision is precisely the argument of the integral $[1 - \prod_j(1 - P_j)]$. This expression has a natural expansion

$$\sigma^{hA}_{\rm prod} = \sum_{\nu=1}^{A}\sigma_\nu, \tag{33}$$

where σ_ν is the cross section for interaction with exactly ν target nucleons

$$\sigma_\nu = \sum_{C(n,A)} \int d^2b \prod_{j\in\{\nu\}} P_j^{hA}(b) \prod_{\ell\in\{A-\nu\}} [1 - P_\ell^{hA}(b)] \tag{34}$$

here the summation is over all possible choices of ν interacting nucleons (among the total A nucleons in the target nucleus) and we use the notation $[j \in \{\nu\}]$ to indicate the running of the index j over the entire set of the interacting ν nucleons, and $[j \in \{A-\nu\}]$ for the running of j over the complementary set of spectator nucleons.

The average number of participating target nucleons per inelastic (with π production) interaction is easily calculable:

$$\langle\nu\rangle = \frac{1}{\sigma_{\rm prod}^{hA}} \sum_\nu \nu\ \sigma_\nu = \frac{A\ \sigma_{\rm inel}^{hp}}{\sigma_{\rm prod}^{hA}} \tag{35}$$

where we have used the identity

$$\sum_{n=1}^{N} n \sum_{C(n,N)} \prod_{j\in\{n\}} X_j \prod_{\ell\in\{N-n\}} (1 - X_\ell) = \sum_{k=1}^{N} X_k \tag{36}$$

that is valid for any integer N and any set of N real numbers $(X_1, \ldots, X_N)$, and then equation (22).

In our code the number of participating target nucleons per inelastic interaction can be easily generated according to the appropriate distribution with a straightforward Monte Carlo method. For each hadron–nucleus collision, a configuration of the target nucleus is generated assigning to each nucleon a position distributed according the appropriate nuclear density. The impact parameter $\mathbf{b}$ of the incident hadron with respect to the center of the nucleus is then generated with a sufficiently wide flat distribution. The program then loops over all target nucleons testing if they are participating in the interaction. The probability of inelastic interaction with the j–th nucleon is $P(|\mathbf{b} - \mathbf{r}_{\perp j}|)$. In case of no interaction a new impact parameter $\mathbf{b}$ is chosen.

4 Inelastic hadron-nucleus interactions

The final step in the development of the model is to extend it to include nuclear effects. Here we treat only interactions of single hadrons in nuclear targets. The simulation of nucleus–nucleus interactions is discussed elsewhere [2].

An important feature of hadron–nucleus interactions is the fact that naive expectations that assume instantaneous particle production are not supported by the data [35]. For example the

average multiplicity of hadron–nucleus interactions is far smaller that what would be generated by a fully developed intranuclear cascade, despite the fact that heavy nuclei appear almost completely 'black' to the projectile particles. A qualitative picture of what is happening is the following [35]. An incident hadron strikes the target nucleus at a given impact parameter and interacts with a nucleon. The incident hadron is excited but essentially remains intact and continues to propagate inside the nucleus, colliding with subsequent nucleons. The projectile emerges from the nucleus having interacted with ν nucleons. The projectile hadron evolves into a multiparticle state over a long distance. Formation of energetic secondaries thus largely occurs outside of the nucleus, with little cascading inside the nucleus. The presence of multiple interactions inside the nucleus does affect the properties of final state hadrons in the projectile region, but much less than what could be naively expected from a intranuclear cascade. As we will discuss in the following string model can describe with good accuracy the effects of these multiple interactions of the projectile particle.

The first crucial ingredient in this calculation is the distribution of ν, the number of participating (or wounded) nucleons in the target nucleus. This distribution was discussed in section 3.3 (see Eq.(34)). The properties of the particles produced in the projectile fragmentation region of a hadron–nucleus collision, will depend on the mass of the target, only through the distribution P_ν.

4.1 String model in nuclei

Application of the string model to hadron nucleus collisions is discussed in Ref. [36]. To describe the algorithms as they are used in SIBYLL, we consider a p–nucleus interaction with c.m. energy $\sqrt{s}$ for each proton–nucleon interaction. A number of wounded nucleons N_W is selected according to the distribution $P_{N_W} = \sigma_{N_W}/\sigma_{inel}^{hA}$. The event is treated as the superposition of $2N_W$ strings, one pair for each wounded nucleon. Each interacting nucleon in the nucleus is split into a quark-diquark pair as in a normal pp interaction. The projectile proton is also split into a quark-diquark pair, which combines with one of the wounded nucleons via two colorless strings exactly as in a proton-proton collision. Pairs of strings to combine with the remaining $N_W - 1$ wounded nucleons are connected with constituents of the sea of the projectile proton. Thus an additional $N_W - 1$ quark–antiquark pairs must be excited from the sea of the incident hadron to combine with the valence quark and diquark components of the remaining wounded nucleons in the target to compose colorless strings.

The joint distribution $\rho(x_1, x_2, \ldots, x_{2N_W})$ of the fractional energy of the beam partons is

$$\rho(x_1, x_2, \ldots, x_{2N_W}) = f_{q_v}(x_1) f_{qq_v}(x_2) f_s(x_3) \ldots f_s(x_{2N_W}) \; \delta \left[1 - \sum_{j=1}^{2N_W} x_j \right], \tag{37}$$

where the three functions $f_{q_v}(x)$, $f_{qq_v}(x)$ and $f_s(x)$ are the distribution of the fractional energy respectively for the valence quark, the valence diquark, and the sea quarks (antiquarks). We have chosen in the case of the proton:

$$f_{uu}(x) \; = \; f_{ud}(x) \; = \; x^{3.0}, \tag{38}$$

with

$$f_{q_v}(x) = [x^2 + \mu^2/s]^{-1/4} \tag{39}$$

and

$$f_s(x) = [x^2 + \mu^2/s]^{-1/2}. \tag{40}$$

Note that the sea quark distribution has the essentially the expected form $\sim x^{-1}$ regulated by an effective 'quark mass' $\mu \simeq 0.3\ GeV$. Note also that Eq. 37 reduces to Eq. 1 when $N_W = 1$ after integration over the diquark variable.

The fragmentation of each of the N_W pairs of strings is assumed to occur as described for hadron-nucleon collisions. We have neglected correlations among interactions on different wounded nucleons, such as might lead to enhanced transverse momentum by successive scattering of the partons of the projectile as it propagates through the nucleus [37]. We have also neglected the Fermi momentum of the nucleons in the target.

The effect of combining the extra $N_W - 1$ wounded nucleons with sea quarks, which carry only a small fraction of the momentum of the projectile, is to insure that the extra multiplicity associated with a collision on a nuclear target is in the backward CM hemisphere, as observed experimentally. This behavior is illustrated in Fig. 12 below. Associated with this extra multiplicity of slow particles is a slight increase in inelasticity. The momentum needed for the $\nu - 1$ $q\bar{q}$ pairs from the projectile is not available for the projectile fragment.

At high energies minijets are added to the hadron nucleus collisions. These are generated for each of the N_W interactions in the same way as in a single hadron-nucleon collision. In particular, the same value $\sqrt{s} = \sqrt{(2m_N^2 + 2m_N E_{\rm Lab})}$ is used for each of the N_W interactions inside the nucleus to calculate the probability from which the number of minijet pairs is chosen.

The only correlation is that the *total* fractional momentum taken from the projectile for jet production cannot exceed an arbitrary value of 0.7. Similarly the total fractional momentum taken from *each* wounded nucleon cannot exceed 0.7.

4.2 Diffractive dissociation on nuclei

We have not attempted to incorporate diffraction dissociation in a completely consistent way into the Glauber multiple scattering formalism. In particular, we do not explicitly include a profile function for "inelastic screening" [38] in the multiple scattering expansion. We use the following classical approximation. A number of participating nucleons, N_A, is chosen randomly for each event from Eqs. 34 and 31. Each of the N_A interactions has a probability $P_{\rm diff} = \sigma_{\rm diff}/\sigma_{inel}$ of being diffractive. Let N_D be the number of diffractive interactions in the collision. If $N_D < N_A$ the collision is non-diffractive with $N_W = N_A - N_D$. If $N_D = N_A$ the event is treated as a diffractive interaction (either beam dissociation, target dissociation or double diffractive dissociation, depending on the character of the N_D diffractive sub-events).

4.3 Summary of inelastic interactions

The steps in the generation of an inelastic hadron-nucleus interaction can now be summarized as follows:

1. Compute $N_A = \nu$ from Eqs. 34 and 31.
2. Decide if the event is diffractive, as described in the previous section. If so generate a dissociation event of the appropriate type (forward, backward or double) and stop.
3. For non-diffractive events, the number of inelastically wounded nucleons is $N_W \leq \nu = N_A$.
4. Continue by selecting the number of minijets, n_i, for each of the N_W inelastically wounded nucleons according to the distributions P_{n_i} given in Eq. 16.
5. Generate the kinematics for each parton-parton interaction according to the parton-parton differential cross sections and the hadron structure functions.
6. Fragment the jet-jet systems according to the fragmentation algorithms.

in the target to compose colorless strings.

7. After the energy for the hard scatterings is removed, we are left with a projectile of energy

$$E = \frac{\sqrt{s}}{2}[\,1 - \sum_{i=1}^{N_W} \sum_{j}^{n_i} x_{i,j}^{(1)}\,] \tag{41}$$

and N_W target nucleons each with energy

$$E_i = \frac{\sqrt{s}}{2}[1 - \sum_{j}^{n_i} x_{i,j}^{(2)}] \tag{42}$$

The remaining energy of each target nucleon is split between the valence quark and valence diquark, and the energy of the projectile is split into $2N_W$ parts: a valence quark, a valence diquark, and $N_W - 1$ $q\bar{q}$ pairs. These partons are joined to produce $2N_W$ colorless strings which fragment into hadrons.

8. The fragmentation algorithm produces the full spectrum of hadrons. A separate routine handles decays of the short lived resonances to leave only final state particles which might re-interact in a cosmic ray cascade, or register in a detector. By default, charged pions and kaons, K_L^0's and nucleons are treated as stable particles.

5 Comparison to accelerator data

In developing this code we aimed to fit simultaneously three sets of experimental data:

(i) Detailed studies of hadron-proton interactions from fixed target experiments ($E_{lab} = 50 - 400$ GeV or $\sqrt{s} = 7 - 30$ GeV).

(ii) High energy $p\bar{p}$ collisions at the CERN and FERMILAB colliders ($\sqrt{s} = 200 - 1800$ GeV).

(iii) Data on fixed target hadron–nucleus interactions.

Data taken in fixed target experiments with beam energies $E_{lab} \sim$ few hundreds of GeV, provide the only possibility to tune the model to experimental results in the fragmentation region, in this energy range the jet cross section is also negligible, so we can test our treatment of soft interactions. Higher energy data from the CERN and Fermilab $p\bar{p}$ colliders help fix the energy dependence of the model. The data on hadron–nucleus interactions, allow tests and tuning of the Monte Carlo algorithms for nuclear interactions. No data is available for hadron–nucleus collisions at higher energy.

5.1 Hadron-nucleon data at fixed target energies

In fixed target experiments, for geometrical reasons, it is possible to study in detail the entire kinematical range for final particles, and also the projectile fragmentation function, which is of particular importance in cosmic ray studies because fast particles, and in particular the leading nucleon, control the rate of energy dissipation in hadronic air-showers. We will discuss a comparison of the SIBYLL output with data on (i) particle composition, (ii) inclusive longitudinal momentum distributions, (iii) inclusive transverse momentum distributions, (iv) charged multiplicity distributions, (v) $p_{||}$-p_T correlations. Obviously there are strong correlations between the different properties of the final state particles, for example harder momentum spectra imply a lower average multiplicity.

5.1.1 Particle composition

The LEBC-EHS experiment on pp collisions at $E_{lab} = 400$ GeV has reported a measurement of the average multiplicity for each type of stable particle, these results are compared to the SIBYLL output in table 1. The average composition of the final state particles is well reproduced by the Monte Carlo algorithms. In the model the relative multiplicities of different particles are fixed by the probability of generating different pairs of parton-antiparton in the fragmentation of the strings and the relative probability of producing scalar or vector mesons, and spin $\frac{1}{2}$ or spin $\frac{3}{2}$ baryons (see section 2.1.1 for a list of the values of parameters chosen). The largest difference between the experimental data and the SIBYLL results is in the average number of protons, the Monte Carlo code produces an average of 1.4 protons per interaction, while LEBC-EHS measures 1.2 ± 0.19.

5.1.2 x_F distribution for charged particles.

The laboratory energy E_{lab} of final particles is closely related to the Feynman-x variable ($x_F = 2p_{||}^{\rm c.m.}/\sqrt{s}$)

$$E_{lab} = \frac{E_0}{2}\left(\sqrt{x_F^2 + \frac{4m_\perp^2}{s}} + x_F\right) \simeq E_0\, x_F \qquad (43)$$

where E_0 is the projectile energy, $m_T = \sqrt{m^2 + p_T^2}$, and the last equality is valid in the forward hemisphere ($x_F \geq 0$) for $x_F \gg 4m_\perp^2/s$. Note also how particles in the backward hemisphere

($x_F \leq 0$) are very soft in the laboratory, and therefore of small importance for the development of showers. The inclusive momentum spectra in the model are constructed as a convolution of the splitting function, that determines how the energy of the initial particle is divided between the two valence components, and the fragmentation function $f(z)$.

Fig. 3 compares the calculated x_F distributions of protons, charged pions and kaons in the forward hemisphere with data at several energies in the range 100–400 GeV (beam energy in the lab system) [39, 40]. The sum of positive and negative particles is represented well. For proton collisions, however, the positive charge excess for $\pi^{\pm}$ and $K^{\pm}$ secondaries is not exactly reproduced at large x_F.

The excess of positive particles has different origins for pions and kaons. The excess of π^+ $[u\bar{d}]$ over π^- $[d\bar{u}]$ is due to the flavor content of the proton $[uud]$. In proton interactions there is also a large excess of K^+, with a much harder spectrum, over K^-. In our model positive kaons $[u\bar{s}]$ can be produced as second rank particles in the fragmentation of a diquark string (in association with the production of a strange baryon), or as first rank particles in the fragmentation of a u–quark string, while negative kaons $[s\bar{d}]$ can only be produced as third rank particles in a diquark string, or as second rank particles in a quark string. The higher *ranking* assures a larger fraction of the string mass and correspondingly a harder x_F distribution for positive kaons. Nevertheless, we have had to tune the string fragmentation function to suppress production of K^- still further relative to K^+ to improve the agreement with the measured ratio at high x_F. The charge ratio of fast kaons is important for the ratio $\nu/\overline{\nu}$ in atmospheric neutrino for energies above $\sim$ 100 GeV. [41, 42]

The spectrum of the 'leading' nucleon is of special importance for the development of high energy hadronic cascades. In our model the leading nucleon is the first rank particle produced in the fragmentation of the color string with a valence diquark attached to the projectile end. To obtain a good agreement between Monte Carlo calculation and the data, (which according to the analysis of Voyvodic [43] indicate a flat x_F distribution) we use a special form $f_L(z)$ of the string fragmentation function for this first rank particle. The exact shape of the proton distribution is also sensitive to the fraction of spin $\frac{3}{2}$ baryons produced, because nucleons produced in the decay of spin $\frac{3}{2}$ baryons are softer than directly generated nucleons. The simulated data show an artificial dip at $x_F \sim 0.85$.

Fixed target experiments offer also the possibility to study meson–nucleon collisions. Fig. 4

shows distributions for all positive and negative particles produced in π–p and K–p collisions, compared to data of Refs. [39, 44]. The general features of the simulated distributions are in good agreement with the measurements. The agreement with data for meson–nucleon collisions shown on Fig. 4 is especially good in the forward hemisphere, which is of primary interest for us. The artificial dips at $x_F \sim 0.8$ is again present in the simulated spectrum. The positive charge excess in π^+–p collisions is well described up to very high x_F values.

5.1.3 Transverse momentum distributions.

It is also very important for our purposes to have a good representation of the transverse momentum distributions of the fastest secondaries that contribute the most to the TeV muon fluxes. The overall transverse momentum distributions of produced particles are determined by the average transverse momenta of quarks produced in string fragmentation (Eq. 2), and by the size of the minijet contribution. Fig. 5-a shows the transverse momentum distributions at 400 GeV from the LEBC–EHS experiment [40] for charged pions and kaons. Our distribution has a slightly softer tail than the LEBC–EHS data. This reflects the assumed Gaussian p_T distribution for string fragmentation, which lacks any high p_T tail. At 400 GeV the energy is too low for minijets to play a role. At collider energy, however, the minijet component does produce a high p_T tail, as shown in Fig. 5-b.

5.1.4 Charged multiplicity distribution.

At fixed target energies the model gives a reasonably good representation of the charged multiplicity. In fig. 6 we show the measured charged multiplicity in pp collisions at $E_{lab} = 250$ GeV, compared with the results obtained with SIBYLL. The Monte Carlo code produces an average charged multiplicity $\langle n_c \rangle = 8.41$, slightly larger than the experimental value (7.88 ± 0.09) [45], with a distribution 16% narrower than the experimental value of $\langle n_c \rangle / \sigma_{n_c} = (1.92 \pm 0.03)$ [45].

The fragmentation of a string of mass M produces an average multiplicity $\propto \ln M$, with a distribution that is approximately Poissonian. In the model a soft nucleon–nucleon interaction is modeled as the production and fragmentation of two color strings with masses M_1 and M_2 determined by the nucleon splitting function. For a given splitting of the two interacting nucleons the multiplicity is: $\langle n \rangle \propto \ln M_1 + \ln M_2 = \ln[s \sqrt{x_{qq}^b(1 - x_{qq}^t)} \sqrt{x_{qq}^t(1 - x_{qq}^b)}]$ where $x_{qq}^{b,t}$ are the fractional energies of the diquarks in the beam and target nucleons. The splitting function

therefore is important in determining the average multiplicity as well as the shape of the multiplicity distribution. We observe that the multiplicity has a maximum for $x_{qq}^{b,t} = 0.5$, that is for symmetric splitting of both nucleons. The broad distribution of x_{qq} result in a multiplicity distribution much broader than a Poissonian. The average multiplicity in the fragmentation of a string is controlled by the fragmentation function $f(z)$ (Eq. 3), and by the probabilities for the production of different flavors and spins. A hard $f(z)$ leads to a lower multiplicity because of energy conservation.

5.1.5 $\langle p_T \rangle$–x_F correlation.

There is a well-known positive correlation between longitudinal and transverse momentum. Because of the shape of the curve of $\langle p_T \rangle$ versus x_F, this effect has become known as the "sea–gull" effect. In the SIBYLL algorithms, a positive correlation of p_T and $|x_F|$ is automatically present for two reasons. The first is that the fragmentation function depends on $m_T = \sqrt{m^2 + p_T^2}$ and becomes harder for particles with larger m_T; a second reason is that in proton interactions, when the projectile particle splits into two valence components, the diquark and quark take transverse momenta that are equal and opposite, with an average $\langle p_T \rangle = 0.45$ GeV determined by a fit to the observed distribution of transverse momentum of fast baryons. As a consequence first rank mesons that have a higher longitudinal momentum than the average particle, have also a higher transverse momentum.

In Fig. 7 we compare LEBC–EHS data ($E_{lab} = 400$ GeV) to the SIBYLL output. The average p_T is shown as a function of x_F for $\pi's$, K's, protons and antiprotons. For x_F below 0.15–0.2 the model follows the rise of transverse momentum with x_F in π and k production seen by the LEBC-EHS collaboration [40]. At higher x_F we underestimate the the rise of $\langle p_T^2 \rangle$. A difference in the $\langle p_T^2 \rangle$ of positive and negative kaons at x_F near 0.1 is seen in the LEBC-EHS data. It most probably comes from the associated production of kaons, which dominates large x_F.

The effect has the same origin for all mesons, and the magnitude decreases with the particle mass. It also shows up for protons where it is quite small. There is an unexpected difference in the p_T–x_F correlation for π^+ and π^-.

5.2 Collider Data

The highest energy data on hadronic collisions comes from the $p\bar{p}$ colliders at CERN and Fermilab. The detectors operating at the colliders can only observe particles produced in the central region, and therefore some of the properties of particle production that are most important for cosmic rays studies, like the energy distribution of the leading baryon or the p_T distribution of fast mesons in the fragmentation region, are not directly measured, however the available data allows several very significant tests of the algorithms of the model.

5.2.1 Charged multiplicity distributions

With increasing c.m. energy, the multiplicity distribution widens. In the minijet model this widening is caused by the production of multiple minijets. In Fig. 8 we show the multiplicity distributions at $\sqrt{s}$ = 200 and 900 GeV, with the contributions from valence strings and from minijets shown separately. The rise in the average number of minijets leads to a rise in the central rapidity density, and contributes to the rise of the total multiplicity.

Although the average charged multiplicity and its energy dependence is well described by the model (see Fig. 10b below) the width of the distributions are consistently underestimated. The experimental values of $\langle n_{ch} \rangle / D$ at the three $\bar{p}p$ collider energies are 1.98$\pm$ 0.02$\pm$.08, 1.87$\pm$0.02$\pm$.08, and 1.82$\pm$0.01$\pm$.10 [9, 46], while SIBYLL returns 2.8, 2.6, and 2.5 at $\sqrt{s}$ of 200, 546 and 900 GeV respectively. It has been shown [47] that the generation of the exact shape of the multiplicity distribution requires a very careful treatment of the fluctuations and correlations in the description of the interaction. The width of the multiplicity distribution depends quite heavily (Fig. 5 in Ref. [47]) on the minimum transverse momentum for gluon jet production. It is also affected by the string geometry and the initial and final state gluon bremsstrahlung.

In high multiplicity events SIBYLL does not create enough soft particles (such as from gluon bremsstrahlung), which will not affect the cascade behaviour. More disturbing is the systematic lack of low multiplicity events, which is emerging in various treatments of the interactions, and has been attributed[47] to a large number of double diffraction events. This seems unlikely to us. In our version of the model the missing low multiplicity events might be related to the dip at x_F ~0.85 in the proton spectrum. We have chosen to sacrifice a better fit of the multiplicity distributions to obtain a relatively good agreement with the x_F spectra.

5.2.2 Pseudorapidity distributions

Fig. 9 shows a comparison with data for the pseudorapidity distribution of charged particles in multiplicity bins at $\sqrt{s} = 200$ and 900 GeV as measured by UA5 [48, 9]. The pseudorapidity density is well described for the major fraction of events. There are problems with the lowest multiplicity bin, probably because in the model it consists almost entirely of double-diffraction, which may shift particles out of the central region acceptance of the experiment.

5.2.3 Transverse momentum distributions

It is well known that the data obtained at the ISR [49] and at the $p\bar{p}$ colliders [50, 51] shows a growth of the average transverse momentum with increasing $\sqrt{s}$. We note that the momentum of particles is measured only in a limited angular region ($|y| \leq 2.5$ for UA1, $|y| \leq 1.0$ for CDF) corresponding to the small x_F in the central region.

In our model a principal reason for the growth of $\langle p_T \rangle$ with energy is the presence of an increasing number of minijets, because the transverse momentum of the hard–scattering partons is shared among the final particles produced in the hadronization of the jets. It must be stressed that because of the kinematical properties of parton–parton scattering, the increase in $\langle p_T \rangle$ is not uniform in longitudinal momentum, but is stronger in the central region, because of the small number of high x partons.

The rise of $\langle p_T \rangle$ with energy due to the increase in production of minijets seems, however, insufficient to account for the observed rise in average transverse momentum observed at the $p\bar{p}$ colliders. For this reason we have also introduced an ad hoc energy dependence into the transverse momentum generated in string fragmentation, as given in Eq. 2. This contribution is independent of x_F and affects uniformly all values of x_F. It is tuned to reproduce the observed rise in average transverse momentum in the central region, as shown in Fig. 10a. The overall transverse momentum distribution at high energy is thus a combination of a Gaussian component and a minijet component, which produces a high p_T tail. This composite distribution is shown in Fig. 5b.

5.2.4 p_T –multiplicity correlation.

The data of the colliders [50, 53] show a positive correlation between multiplicity and p_T. The minijet model intrinsically contains such a positive correlation because events where one or more

hard parton scatterings are present (even if not recognizable as identified jet pairs), will have a larger than average multiplicity, and also a larger transverse momentum.

In Fig. 11 we show the calculated $\langle p_T \rangle$ as a function of the charged multiplicity density, compared to UA1 data [50] for $|\eta| < 1$. The model overestimates the average p_T in the low multiplicity region, where it also produces too few events. The upper panel in Fig. 11 shows the relative number of events as a function of rapidity density. Comparison of the two curves shows that the mean p_T is correct for most events.

5.3 Hadron-nucleus data

The amount of data on hadron–nucleus collisions available for tuning the Monte Carlo algorithms is less than for hadron–proton interactions. A first important feature of hadron–nucleus collisions is the softening of the leading particle, which increases for larger target masses. In Fig. 12 we show the distribution of x_F of final protons for proton collisions on beryllium, copper and silver targets at $E_{lab} = 100$ GeV [34]. The agreement is not perfect, but the softening of the proton spectrum is reasonably well described.

In Fig. 13 we show a plot of the ratio of the rapidity densities in proton–nucleus interactions to those in proton–proton interactions. The data are for 200 GeV/c protons from Ref. [54]. For a nuclear target, the rapidity density increases in the target hemisphere, because on average more than one target nucleon participates in the interaction. Conversely, the density of large rapidity particles in the projectile hemisphere is suppressed.Both these phenomena are qualitatively well reproduced by the model.

For rapidities close to the kinematical limit in the target hemisphere, the data show a large enhancement in the density of final particles. These are target fragments, including products of reinteraction and cascading in the target nucleus of those particles that have a rapidity close to the target nucleons. In the SIBYLL code there is no attempt to model these processes, because particles in this kinematical region are nearly at rest in the laboratory frame and therefore have negligible importance in the development of a shower.

For rapidities near the beam, the production on nuclear targets in SIBYLL is comparable to that on protons, as shown by the increase of the nuclear/proton histogram in the highest two bins of rapidity in Fig. 13. The data on argon appear to show this feature, but not the xenon data.

6 Energetic muons

The purpose of this section is to illustrate the application of SIBYLL to a problem of current interest, the rates of coincident muons in deep underground detectors such as Frejus [55], Soudan [56], MACRO [57, 58] and LVD [59]. We will also compare results obtained with SIBYLL to those obtained with the interaction model of HEMAS [1]. The minimum energy at production required for a muon to reach these detectors is 2 to 3 TeV (except for Soudan, where the threshold is 0.6 TeV). The principal physics interest of the underground muons is the composition of the primary cosmic ray beam in the region of the knee of the spectrum (10^{14} to $> 10^{16}$ eV). To probe this high energy region it is necessary to look at events of high multiplicity. The dominant contributions to the rate of muon events underground are events of low multiplicity, particularly the rate of single muons. These are useful as a probe of the primary energy spectrum at lower energy ($\sim$ 10 TeV) where there are overlapping direct measurements. The measured rate of single muons also serves to calibrate the detector, including the map of the overburden.

6.1 Inclusive muon flux

Calculations of the fluxes of muons in the atmosphere [60, 61, 62, 41] all depend on the assumed primary spectrum of nucleons and on the inclusive cross sections for pion and kaon production. It is useful to characterize the inclusive cross sections by their moments, weighted by the shape of the primary spectrum. In particular, the contribution of pions is approximately proportional to

$$Z_{p\pi^{\pm}} = \int_0^1 x^{\gamma} \frac{\mathrm{d}N_{p\pi}}{\mathrm{d}x} \mathrm{d}x, \tag{44}$$

where $\mathrm{d}N/\mathrm{d}x$ is the distribution of charged pions produced in collisions of protons with nuclei in the atmosphere, $x = E_{\pi}/E_p$ and γ is the spectral index of the primary cosmic ray spectrum. The corresponding factors $Z_{pK^{\pm}}$ (for production of charged kaons), Z_{pK^0}, $Z_{p\pi^0}$, Z_{pp}, are defined analogously.

The spectrum weighted moments appear explicitly in analytic approximations to the uncorrelated particle fluxes in the atmosphere [42]. The Z–factors also provide a good measure of the shape of the inclusive cross sections, which is relevant to energy flow in air showers. A knowledge of these moments therefore provides useful insights into the results of complex Monte Carlo simulations.

Table 2 compares the Z–factors generated by SIBYLL at several energies to the Z–factors from the HEMAS program, which has previously been used to calculate the fluxes of underground muons. The Z–factors show the basic characteristics expected from the model. Central minijet production causes scaling violations, which softens the x_F spectra of produced mesons and causes a slow drop in the Z factors. The Z–factor for charged pion production in SIBYLL is about 15% larger than in the HEMAS model at 10 TeV, whereas the factor for charged kaons is 30% higher in HEMAS. If $\sim$ 20% of $\geq$TeV muons come from kaon decay [42] we can then estimate that the inclusive muon flux calculated with SIBYLL should be about 7% higher than with HEMAS.

Palamara & Petrera[63] have made a simulation of muons that reach the depth of MACRO, keeping track separately of muons with kaon parents and those with pion parents. They have performed the simulations both with SIBYLL and with the interaction model of HEMAS. It is interesting to use their calculated partial rates, together with the Z-factors from Table 2 to understand the difference in the rates of inclusive muons calculated in the two models. (The inclusive muons are dominated by single muons at the level of the detector.) This comparison is made in Table 3, which shows the muon rates calculated [63] at MACRO separately for pion parentage and for kaon parentage. The middle column shows the rates calculated with SIBYLL and corrected by the ratio of Z-factors, which is consistent with the partial rates calculated using HEMAS (column 3).

6.2 Multiple muons

The distribution of the number of events with N muons having $E_\mu > 1$ TeV is shown in Fig. 14 for SIBYLL and HEMAS. The singles rate is higher for SIBYLL, as explained above, but the rates of multiples are higher for HEMAS. The example shown in Fig. 14 was produced from proton primaries with an $E^{-2.7}$ differential energy spectrum. The same general trend appears in the more realistic comparison of the two models made by Palamara & Petrera [63]. They have used primary spectra which contain a fraction of heavy nuclei as well as protons (the "light" and "heavy" spectra of Ref. [57]). They find that the multiplicity distributions of muons at MACRO calculated in with the two models has a similar behavior to Fig. 14, with single muons slightly higher in SIBYLL and multiple muons slightly higher with HEMAS. The single muons (and the inclusive muon rates) are dominated by proton primaries, whereas the high multiplicity events come predominantly from heavy primary nuclei. The separation between the two models for high multiplicities is smaller in the more realistic comparison of Palamara and Petrera, presumably

because of the predominant contribution of heavy nuclei to the events of high multiplicity, which are not present in Fig. 14 here. (Heavy nuclei are treated in the semi-superposition model of Ref. [2].)

Lateral distributions of ~TeV muons in showers are slightly broader with the HEMAS interaction model than with SIBYLL, as indicated by the mean values in Table 4. The values listed in the table are for proton-initiated showers of fixed energy. The quantity $\langle r \rangle$ is the mean separation of muons from the shower core. This quantity is dominated by events with $N_\mu = 1$, especially at low energy and so is only of technical interest. Of more practical interest is the mean separation between pairs of muons. In calculating $\langle r_{\rm pair} \rangle$, independent pairs are weighted by $2/N_\mu(N_\mu - 1)$, as in Ref. [58]. We note that the relation $\langle r \rangle < \langle r_{\rm pair} \rangle / \sqrt{2}$ because $\langle r \rangle$ includes events with only one muon.

The difference in the predicted lateral spread of muons in showers calculated with the two models arises from the difference in their treatment of the transverse momentum of produced pions. In Fig. 15 we compare the mean transverse momentum produced in proton–air interactions in the two models. For $x_{\rm lab} < 0.05$ they give the same value because both are tuned to reproduce the observed rise in transverse momentum in the central region. For larger x, however, $\langle p_T \rangle$ is significantly greater in HEMAS.

7 Showers at Fly's Eye energy

The main feature of the minijet model as represented by SIBYLL that affects development of high energy cascades is the inelasticity. Inelasticity here is defined as the fraction of energy not carried off by the nucleonic fragment of the projectile nucleon. The spectrum of the leading nucleon can be obtained in practice by subtracting the inclusive cross section for $p + \text{air} \to \bar{N} + \text{anything}$ from that for $p + \text{air} \to N + \text{anything}$. The inelasticity increases with energy and is larger on a nuclear target than on nucleons. The inelasticity for proton-air as well as for proton-proton collisions is listed in Table 2 along with the Z-factors.

A preliminary version of SIBYLL has been used as part of an analysis of the Fly's Eye measurement of the distribution of shower maximum for showers in the energy range 10^{17} to 10^{19} eV [64]. The event generator used there [65] was a version of Hillas' splitting algorithm [66] with an energy-dependent number of pre-splittings to match the shape of the inclusive hadron-nucleus cross sections produced by a preliminary version of SIBYLL. In Table 5 we compare the

mean depth of maximum ($\langle X_{\rm max}\rangle$ obtained with the full SIBYLL to that used in Ref. [64]. The agreement is satisfactory, although the elongation rate 5% larger for SIBYLL than in Ref. [65].

The elongation rate is defined as the slope of $\langle X_{\rm max}\rangle$ *vs.* the logarithm of the energy of a shower. For a purely electromagnetic cascade the elongation rate is equal to the radiation length in air, which is 37 g/cm^2 or 85 g/cm^2 per decade of energy. The elongation rate is also equal to the radiation length for a hadronic cascade as a function of energy per nucleon, provided there are no scaling violations, i.e. constant cross section and Feynman scaling for the inclusive cross sections.

It is instructive to trace how the elongation rate goes from the naive scaling value of 85 g/cm^2 to a number like 58 in SIBYLL. This can be done by turning on the factors that cause scaling violation one-by-one, after first checking that a pure scaling model with constant cross sections indeed gives the expected value of 85. There are three steps: [65]

1. The elongation rate decreases from 85 to 72 when the increasing cross section is turned on. This is confirmed by the result of Hillas [67, 68], the column labelled MOCCA92 in Table 4. He finds an elongation rate of 71 g/cm^2 in a model which uses a scaling representation of data from proton-proton interactions with an energy-dependent cross section.

2. Next, scaling violation is turned on by adding minijets to proton-proton collisions. The elongation rate decreases from 72 to 65.

3. Finally, the nuclear target effect is added and the elongation rate decreases further to 55 g/cm^2 per decade.

Because of the way the number of wounded nucleons is computed (see §3.3), turning on the nuclear target amplifies the increase with energy of both the hadron-proton cross section and the probability of minijet production.

Since the depth of shower maximum depends on energy per nucleon,

$$\langle X_{\rm max}\rangle \propto \log\left(\frac{E}{A}\right), \tag{45}$$

the observed elongation rate can also be affected by a change with energy in the elemental composition of the primary cosmic radiation. This is evidently the case with the Fly's Eye experiment [64]. The showers are observed to develop very high in the atmosphere (i.e. small value of $X_{\rm max}$). This requires both a large fraction of heavies and a highly inelastic interaction

model. At the same time, the observed elongation rate is 79 ± 3 between 3×10^{17} eV and 10^{19} eV. This requires a transition from very heavy composition at the bottom of this energy range to a large fraction of protons at the top end.

8 Conclusion

In this paper we have addressed two related problems. The first is the problem of developing a correct and precise algorithm for the Monte Carlo generation of hadron–nucleus and nucleus–nucleus interactions at high energy. The development of such a model is a necessary ingredient for many studies of high energy cosmic rays and high energy astrophysics. The second problem is the development of an understanding of the features and structure of high energy hadron interactions as an important scientific goal *per se*. A consistent theoretical framework to describe the hadronic interactions is necessary for cosmic ray studies because one needs to extrapolate (in c.m. energy, kinematical region and target type) from the existing data, and a 'motivated' extrapolation is desirable.

The development of such a theoretically motivated model requires putting together perturbative calculations (that describe well the production of high p_T jets) with non–perturbatively–calculable features of the interactions. The minijet model is a simple and economical one that is suitable for analytic and Monte Carlo calculations and that predicts effects such as growth of the cross sections, increase of $\langle p_T \rangle$, and rise of the rapidity plateau, in qualitative agreement with the data. We use the dual parton model to describe the soft background for minijets as well as nuclear effects. With the parameters tuned to fit observed features, such as the rise with energy of the cross section, the increase of transverse momentum, the correlation between transverse momentum and energy and the production of minijets, the model could then be used to extrapolate to regions of energy and parameter space beyond the data. The effort is only partially successful at present. There are two important limitations:

1. The addition of minijets was insufficient to produce the increase in $\langle p_T \rangle$ observed between fixed target and collider energies.

2. The low energy behavior of the inelasticity and some related features of the model are not in precise agreement with data. In fact, for technical reasons, SIBYLL should not be used below $E_{\rm lab} = 100$ GeV.

We want to stress that our Monte Carlo implementation of the 'ansatz' of the minijet model is very simple and several 'improvements' are possible.

(i) We consider that the parton–parton scattering has a sharp threshold, $Q^2_{\rm min}$, below which hard interactions are neglected and above which they are simply treated using the 1st order Born expression for the cross section. This is an unrealistic approximation, since we expect a smooth passage from the non–perturbative to the perturbative regime. A more sophisticated treatment of the threshold effects would modify the details of the high energy effects.

(ii) For simplicity and speed we also treat each jet–jet system as an independent, colorless string system that fragments uncoupled from the rest of the event (apart from obvious – and important – kinematical constraints). A possible complication of the model would be to consider that in general two scattering partons will carry a net color, and therefore the jet–jet systems could be dynamically coupled to the fragmentation region in more complex ways, as discussed for example by Sjöstrand & van Zijl [47]. An additional improvement would be to consider initial and final state radiation for the scattering partons, and include in the model the formation and fragmentation of multiparton systems.

(iii) An attractive feature of the minijet model is that it implies a relation between the inelastic cross section and several properties of the final state particles (e.g. average multiplicity, average transverse momentum, ...), because all these quantities depend on the average number of minijets pairs per inelastic event. In our model the energy dependence of $\langle n_{jet} \rangle$ is simply and completely determined by the parameters $Q^2_{\rm min}$ and the K–factor. It can be argued that because of the simplicity of the inclusion of hard interactions in our scheme, such a constraint should be abandoned, leaving more flexibility in fitting the data at the expense of a less controlled extrapolation in energy. Additional complications are the possible energy dependence of σ_{soft} and the shape of the profile function $A(b)$.

To reproduce the observed energy-dependence of the transverse momentum, we had to introduce an arbitrary logarithmic increase of the $\langle p_T \rangle$ parameter for string fragmentation in Eq. 2. This 'soft' increase of $\langle p_T \rangle$ in addition to the increase due to minijet production, is purely phenomenological and not theoretically motivated. It is unclear if the need for the inclusion of this effect is due to the approximations that we have used in the implementation of the minijet 'ansatz' or due to a more fundamental problem. In practice, this is not a serious problem for analysis of the multiple muon data because those data do not probe energies very far beyond

the collider energies ($\sqrt{s}$ = 1.8 TeV or $E_{\rm lab} \sim$ 2 PeV/nucleon). The extrapolation to Fly's Eye energies is uncontrolled. Here, however, lateral spread of air showers is primarily controlled by the many lower energy interactions in the cascade. (In addition, Fly's Eye itself does not at present measure lateral structure of events.)

Some of the difficulties encountered by our model are related not so much to the 'minijet ansatz' but to the low energy model (based on the dual parton model) over which the hard interactions are superimposed. At low energies ($E_{\rm lab} \lesssim$ 300 GeV) the model predicts the production and fragmentation of low mass color strings. Because of technical difficulties in the fragmentation of these low mass systems, the model produces some undesired kinematical effects resulting in a low energy behaviour of the inelasticity and other related quantities that is not in precise agreement with data. The same features of the model prevent it from giving a good representation of the low multiplicity part of the charged multiplicity distribution for non-diffractive events. We consider these problems to be less serious than the transverse momentum problem mentioned above because the model does give a reasonable behavior of the inelasticity at higher energies.

We would like to remark that, apart from the increase in average transverse momentum, all parameters of the model are energy independent. The energy dependence is generated by the opening up of phase space for minijet production, convoluted with the nuclear target effects, rather than from any energy-dependence of the parameters themselves. Including additional energy dependence, for example of the string fragmentation parameter, would result in a better agreement of the model with some features of the existing data, but at the expense of the introduction of some arbitrariness in the extrapolation to high energy. This consideration should be taken into account in comparing our results, which try to fit many pieces of data obtained at different c.m. energy and with different projectiles and targets, with other Monte Carlo calculations that attempt to fit only a fraction of the existing data. We also note that in the process of choosing the best parameters of the models we did need to compromise because the various features of the interactions are all very closely correlated with each other. Changing the value of a parameter to improve one aspect (e.g. the momentum distribution of the leading nucleon) can adversely affect other properties (e.g. the multiplicity distribution and the charge ratio of fast mesons).

Apart from the transverse momentum problem, the model gives a good representation of the data and extrapolates in a reasonable fashion to high energy. In particular, the dependence of inelasticity on energy and target mass displayed in Table 2 embodies correctly the qualitative features of the model, which are distinctly different from the corresponding behavior of the MAS interaction model, where the inelasticity decreases slightly with energy rather than increasing. We believe therefore that use of SIBYLL in in comparison with other models will be valuable in analysis of cosmic ray cascade data above 100 TeV.

ACKNOWLEDGMENTS. We are grateful to L. Voyvodic for helpful discussions of properties of hadronic interactions on nuclear targets. We thank Giuseppe Battistoni, A.M. Hillas, Sue Kasahara, Ornella Palamara, John Petrakis and Sergio Petrera for trial runs of SIBYLL in the context of their own data analysis efforts and for many helpful discussions. This work is supported in part by the U.S. Department of Energy. RSF thanks the particle theory group at Johns Hopkins University where part of this work was completed, and particularly Jon Bagger for his hospitality.

References

[1] C. Forti *et al.*, *Phys. Rev.* **D42**, 3668 (1990). HEMAS refers both to a cascade code and to an interaction model or event generator, whereas SIBYLL refers only to the hadronic event generator. The structure of the cascade code is modular so that, for example, the HEMAS interaction model can be replaced by SIBYLL to isolate the effects of differences in interaction model on cascade properties.

[2] J. Engel, T.K. Gaisser, Paolo Lipari and Todor Stanev *Phys. Rev.* **D46**, 5013 (1992).

[3] A.Capella and A. Krzywicki, Phys.Rev. D18, 3357, (1978); A.Capella and J.Tran Thanh Van, Zeit. Phys. C10, 249, (1981).

[4] T.K. Gaisser and F. Halzen, Phys.Rev.Lett. 54, 1754, (1985); Pancheri & Srivastava, Phys.Lett. 159b, 69, (1985);

[5] L. Durand and H. Pi Phys.Rev.Lett. 58, 303, (1987); Phys.Rev. D 38, 78, (1988);

[6] H.Bengtsson and T.Sjöstrand Comp.Phys.Comm. 46, 43, (1987).

[7] X.N. Wang an M. Gyulassy, Phys.Rev. D 44, 3501, (1991); 45, 844, (1992);

[8] K.Werner Phys.Rev. *D39*, 780, (1989). See also K. Werner, *Phys. Reports* **232**, 87 (1993).

[9] UA5 collaboration, G.J.Alner et al. Phys.Rep. 154, 247, (1987).

[10] B.Andersson et al., Phys.Rep. 97, 31, (1983).

[11] R.S. Fletcher, T.K. Gaisser, Todor Stanev & Paolo Lipari, *Proc. 22nd Int. Cosmic Ray Conf.* (Dublin) vol. 4, p. 193 (1991).

[12] For a study of diffractive dissociation in the minijet model using a Good-Walker [13] formalism, see R.S. Fletcher *Phys. Rev.* **D46**, 187 (1993).

[13] M.M. Good & W.D. Walker, *Phys. Rev.* **120**, 1857 (1960).

[14] Y.Akimov et al., Phys.Rev. D14, 3148, (1976).

[15] K.Goulianos, Phys.Rep. 101, 3, (1983). Nuc. Phys.. B (Proc.Suppl.) 12, 110, (1990).

[16] UA4 Collaboration, D. Bernard *et al.*, *Phys. Letters* **166b**, 459 (1986).

[17] UA1 collaboration, C.Albajar et al. Nucl.Phys. B309, 405, (1988).

[18] T.K.Gaisser and T.Stanev, Phys.Lett.B219, 375, (1989).

[19] D. Cline, F. Halzen and J. Luthe, Phys.Rev.Lett.31, 491, (1973).

[20] E.J. Eichten, I. Hinchliffe, K. Lane and C. Quigg, Rev. Mod. Phys.56, 579, (1984).

[21] L. V. Gribov,E.M. Levin and M.G. Ryskin, Phys.Rep. 100, 1, (1983).

[22] J.F. Owens, Phys.Rev. D30, 943, (1984).

[23] L. Durand & R. Lipes, *Phys. Rev. Lett.* **20**, 637 (1968).

[24] T.T. Chou & C.N. Yang, *Phys. Letters B* **128**, 457 (1983).

[25] L. Durand & H. Pi, *Phys. Rev.* **D40**, 1436 (1989).

[26] B. Margolis, P. Valin, M.M. Block, F.Halzen and R.S. Fletcher, Phys. Lett. **B213** 221 (1988).

[27] P. Lipari, submitted to *Phys. Rev. D.*

[28] M.M.Block and R.N.Cahn, Rev.Mod.Phys. 57, 563, (1985).

[29] E710 collaboration, N.A.Amos et al. Phys.Lett. 243B, 158, (1990).

[30] R.J. Glauber, *Nucl. Phys.* **B21**, 135 (1970).

[31] R.J.Glauber and G.Matthiae, Nucl. Phys. B21, 135, (1970).

[32] R.C. Barrett and D.F. Jackson, "Nuclear sizes and Structure" (Oxford University, New York, 1977).

[33] T.K.Gaisser, U.P.Sukhatme and G.B.Yodh Phys.Rev. *D36*, 1350, (1987).

[34] R. Bailey et. al. Zeit. Phys. C29, 1, (1985).

[35] E.M. Levin and M.G. Ryskin, LINP Preprint 1246 (1987).

[36] A.Capella et al., Zeit. Phys. C33, 541, (1987).

[37] D. Antreasyan et al., *Phys. Rev.* **D19**, 764 (1979).

[38] V.A. Karmanov and L.A. Kondratuk *Pis'ma Zh. Eksp. Teor. Fiz.* **18**, 451 (1973) [JETP Lett. **18** 226, (1973)]

[39] A.E.Brenner et al., Phys.Rev. D26, 1497, (1982).

[40] LEBC-EHS collaboration, M. Aguilar-Benitez et al. Zeit. Phys. C50, 405, (1991).

[41] V. Agrawal, T.K. Gaisser, Paolo Lipari and Todor Stanev, in preparation.

[42] Paolo Lipari, Astroparticle Physics 1, 195, (1993)

[43] L.Voyvodic, *Proc. VII Int. Symp. on Very High energy Cosmic Ray Int*, Ann Arbor, 231, (1992).

[44] EHS-NA22 collaboration, M. Adamus et al. Zeit. Phys. C39, 311, (1988).

[45] EHS-NA22 collaboration, Adamus et al. Zeit. Phys. C32, 475, (1986).

[46] UA5 collaboration, G.J. Ansorge et al. Zeit. Phys. C43, 357, (1989).

[47] T. Sjöstrand and M. van Zijl, Phys.Rev. D36, 2019, (1987).

[48] UA5 collaboration, G.J.Alner et al. Zeit. Phys. C33, 1, (1986).

[49] P.Capiluppi *et al.*, Nucl.Phys. B 70, 1, (1974). (ISR data)

[50] UA1 collaboration, G.Arnison *et al.* Phys.Lett. B 118, 167 (1982).

[51] CDF collaboration, F.Abe *et al.* Phys.Rev.Lett. 61, 1819, (1988).

[52] UA1 collaboration, C. Albajar et al. Nuc. Phys. B355, 261, (1990).

[53] T.Alexopoulos *et al.* (E735 experiment), Phys.Rev.Lett. 61, 1819, (1988).

[54] Demarzo et al. Phys. Rev. D26, 5, (1982).

[55] Ch. Berger et al. (Frejus Collaboration) Phys.Rev. D40, 2163, (1989).

[56] W.W.M. Allison et al. HE 4.0.3, *Proc. 23'rd Int. Cosmic Ray Conf*, (Calgary) 4, 398, 1993.

[57] S. Ahlen et al. (MACRO Collaboration) Phys.Rev. D46, 895, (1992) and O. Palamara et al. (MACRO Collaboration), Proc. 23rd Int. Cosmic Ray Conf. (Calgary) vol. 2, 97 (1993).

[58] S. Ahlen et al. (MACRO Collaboration) Phys.Rev. D46, 4836, (1992) and C. Bloise et al. (MACRO Collaboration) Proc. 23rd Int. Cosmic Ray Conf. (Calgary) vol. 2, 93 (1993).

[59] G. Bari *et al.* (LVD Collaboration) *Nucl. Inst. Methods* **A277**, 11 (1989).

[60] L.V. Volkova, Sov. J. Nuc. Phys. 31, 1510, (1980).

[61] K. Mitsui, Y. Minorikawa and H. Komori Nuovo Cimento, 9C, 995, (1986).

[62] A.V. Butkevich, L.G. Dedenko and I.M. Zheleznykh Sov. J. Nuc. Phys. 50, 90, (1989).

[63] Palamara and Petrera, private communication.

[64] T.K. Gaisser et al. Phys. Rev. D47, 1919, (1993). See also D.J. Bird et al. (Fly's Eye Collaboration) Phys. Rev. Lett. 71, 3401, (1993).

[65] Serap Tilav, Ph.D. Thesis University of Delaware 1991. This form was used in Ref. [64]

[66] A.M. Hillas. *Proc. 16th Int. Cosmic Ray Conf*, (Tokyo) **8**, 7, 1979.

[67] A.M. Hillas, private communication.

[68] R.S. Fletcher et al. *Proc. 23'rd Int. Cosmic Ray Conf*, (Calgary) **4**, 40, 1993.

FIGURE CAPTIONS

Fig. 1. Fig. 1. shows the total (tot), inelastic (inel), single (sd) and double (dd) diffractive cross section used in SIBYLL, for pp (left frame) and πp interactions. The dashed curve is the minijet cross section, as described in the text. The data are shown for total, inelastic and single diffractive cross sections. References for the low energy data are cited in Ref. [28]. The high energy data is from Ref. [29]. For $\sqrt{s} > 100$ GeV the data are from $\bar{p}p$ collisions.

Fig. 2. Total (tot), production (prod), elastic (el), and quasielastic(qe) cross sections for p–air, and π–air scattering in SIBYLL.

Fig. 3. The histograms show the SIBYLL x_F distributions for proton-proton scattering at 400 GeV in the lab: a) positive and negative pions, b) charged pions, c) positive and negative kaons, and d) protons and antiprotons. The data are from Ref. [40] at 400 GeV/c, and from [39] at 100 and 175 GeV/c.

Fig. 4. Histograms show the SIBYLL x_F distributions for meson–proton collisions at 250 GeV/c: a) positive and negative charged particles and b) forward positive and negative pions in π^+p reactions; and c) positive kaons in K^+p reactions. The data are from a) Refs. [44], and b,c) Ref. [39].

Fig. 5 Transverse momentum distributions for positive and negative pions and kaons, at a) $E_{\rm lab} = 400$ GeV and b) for all charged particles at $\sqrt{s} = 546$ GeV. The data are from a) Ref. [40] and b) Ref. [52] for $-1 \leq y \leq 1$.

Fig. 6. Sibyll charged multiplicity distributions compared to data for pp collisions at $E_{\rm lab} =$ 250 GeV [44].

Fig. 7 shows the average p_T as a function of x_F for pp collisions at $E_{\rm lab} = 400$ GeV. The panels show curves for positive (solid) and negative (dashed) a) $\pi's$, b) k's, and c) protons.

Fig. 8. Charged multiplicity distributions in $\bar{p}p$ collisions at $\sqrt{s}$ =200 and 900 GeV, [46]. Contributions are shown separately for no-jet events and for events with minijet production.

Fig. 9. Pseudo-rapidity distributions for fixed multiplicity intervals for a) $\sqrt{s}$ =200, and b) 900 GeV. From bottom to top, multiplicity ranges included are, [2 to 10], [12 to 20], [22 to 30], [32 to 40] and [42 to 50]. At 200 GeV (a) the highest set is for $N_c > 52$; at 900 GeV (b) the highest two curves are for [52 to 60] and [62 to 70].

Fig. 10. SIBYLL predictions for a) average transverse momentum and b) average multiplicity of charged particles as a function of center of mass energy in pp collisions are shown as solid lines. The data is from Ref. [9], and Ref. [52].

Fig. 11. The p_T multiplicity correlation in SIBYLL, compared to data from UA1 [50] (lower panel). The upper panel shows the relative contribution of the different classes of events to the overall interaction cross section.

Fig. 12. SIBYLL proton distributions (solid lines) for proton interactions on Be, Cu, and Ag, compared to data from Ref. [34]. As in pp collisions, SIBYLL shows some overproduction of protons.

Fig. 13. The ratio of the rapidity distributions with nuclear targets as compared to proton targets:

$$R(p/A) = \frac{[dN/dy(pA \rightarrow charged + X)]}{[dN/dy(pp \rightarrow charged + X)]} \tag{46}$$

The center of mass of the system is a y=3. The data is from Ref. [54].

Fig. 14. Multiplicity of muons above 1 TeV at ground level, from vertical showers due to primary protons between 1 and 10^6 TeV distributed on a $E^{-2.7}$ differential spectrum. Solid histogram: SIBYLL; dashed histogram: HEMAS. Both sets are obtained using the same (HEMAS) cascade code so that differences are due only to the different representation of the hadronic interactions.

Fig. 15. $< p_T >$ as a function of x_F, at 100 (upper) and 10 (lower) TeV, in the SIBYLL (solid) and HEMAS (dashed) models.

Table 1: Average multiplicity of final state particles in the forward hemisphere ($x_F \geq 0$), for pp interactions with $E_{lab} = 400$ GeV.

	π^0	π^+	π^-	K^+	K^-	p	$\bar{p}$
SIBYLL	1.81	2.00	1.67	0.17	0.12	0.17	0.038
LEBC-EHS	1.94 ± .06	2.05 ± .055	1.67 ± .04	0.166 ± .08	0.112 ± .055	0.60 ± .097	0.031 ± .001

Table 2: Z–factors at high energy for *p-air* interactions.

	SIBYLL					HEMAS Ref. [1]			
Energy	$Z_{p\pi^\pm}$	$Z_{pK^\pm}$	Z_{pN}	K_{in}^{pA}	K_{in}^{pp}	$Z_{p\pi^\pm}$	$Z_{pK^\pm}$	Z_{pN}	K_{in}^{pA}
1 TeV	0.072	0.0073	0.27	.61	.55	.060	.0094	.26	.60
10 TeV	0.068	0.0071	0.28	.60	.54	.060	.0099	.26	.60
10^2 TeV	0.067	0.0070	0.28	.61	.54	.059	.0010	.28	.59
10^3 TeV	0.066	0.0070	0.26	.63	.55	.060	.0010	.29	.58
10^4 TeV	0.065	0.0070	0.24	.65	.57	.060	.0011	.30	.57
10^5 TeV	0.063	0.0068	0.22	.68	.58	.060	.0012	.32	.55

Table 3: Comparison of partial inclusive muon rates (in units $10^{-4}/\mathrm{m}^2\mathrm{s\ sr}$).

	SIBYLL	SIBYLL$\times Z_H/Z_S$	HEMAS
$\pi \to \mu$	0.61	0.53	0.51
$K \to \mu$	0.133	0.176	0.171

Table 4: TeV Muon production in HEMAS and SIBYLL for fixed energy primaries.

	SIBYLL				HEMAS Ref. [1]			
Energy	$\langle n \rangle$	$\langle r \rangle$ (m)	$\langle r_{\rm pair} \rangle$ (m)	$\langle h \rangle$ (km)	$\langle n \rangle$	$\langle r \rangle$ (m)	$\langle r_{\rm pair} \rangle$ (m)	$\langle h \rangle$ (km)
10 TeV	0.054	6.85	13.3	19.6 km	.056	8.56	15.5	19.4
100 TeV	0.58	4.94	8.32	16.6	0.67	5.40	8.87	16.6
1000 TeV	3.35	3.89	5.61	13.7	3.58	4.13	5.98	13.1

Table 5: Average depth of shower maximum (gm/cm^2).

Energy (eV)	Sibyll	Tilav et. al.	MOCCA92
10^{15}	$598. \pm 1.9$	$601. \pm 2.0$	$591. \pm 4.0$
10^{16}	$654. \pm 1.7$	$660. \pm 1.8$	—
10^{17}	$713. \pm 1.4$	$712. \pm 1.4$	$733. \pm 2.0$
10^{18}	$770. \pm 1.3$	$766. \pm 1.3$	$800. \pm 2.0$
10^{19}	$831. \pm 1.2$	$819. \pm 1.1$	$861. \pm 2.0$

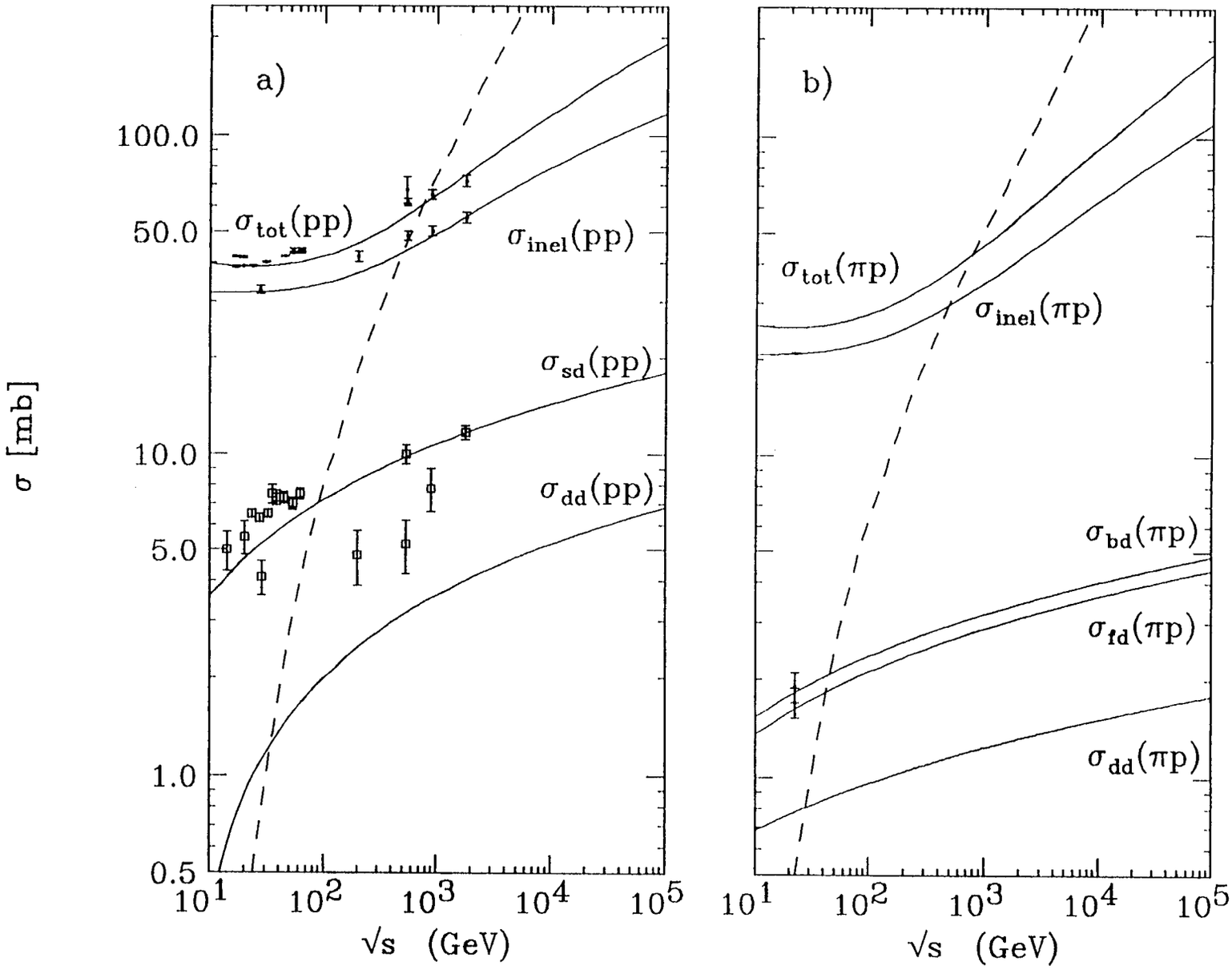
a)
b)
σ [mb]
100.0
50.0
10.0
5.0
1.0
0.5
$\sigma_{tot}(pp)$
$\sigma_{inel}(pp)$
$\sigma_{sd}(pp)$
$\sigma_{dd}(pp)$
$\sigma_{tot}(\pi p)$
$\sigma_{inel}(\pi p)$
$\sigma_{bd}(\pi p)$
$\sigma_{fd}(\pi p)$
$\sigma_{dd}(\pi p)$
10^1
10^2
10^3
10^4
10^5
√s (GeV)
√s (GeV)

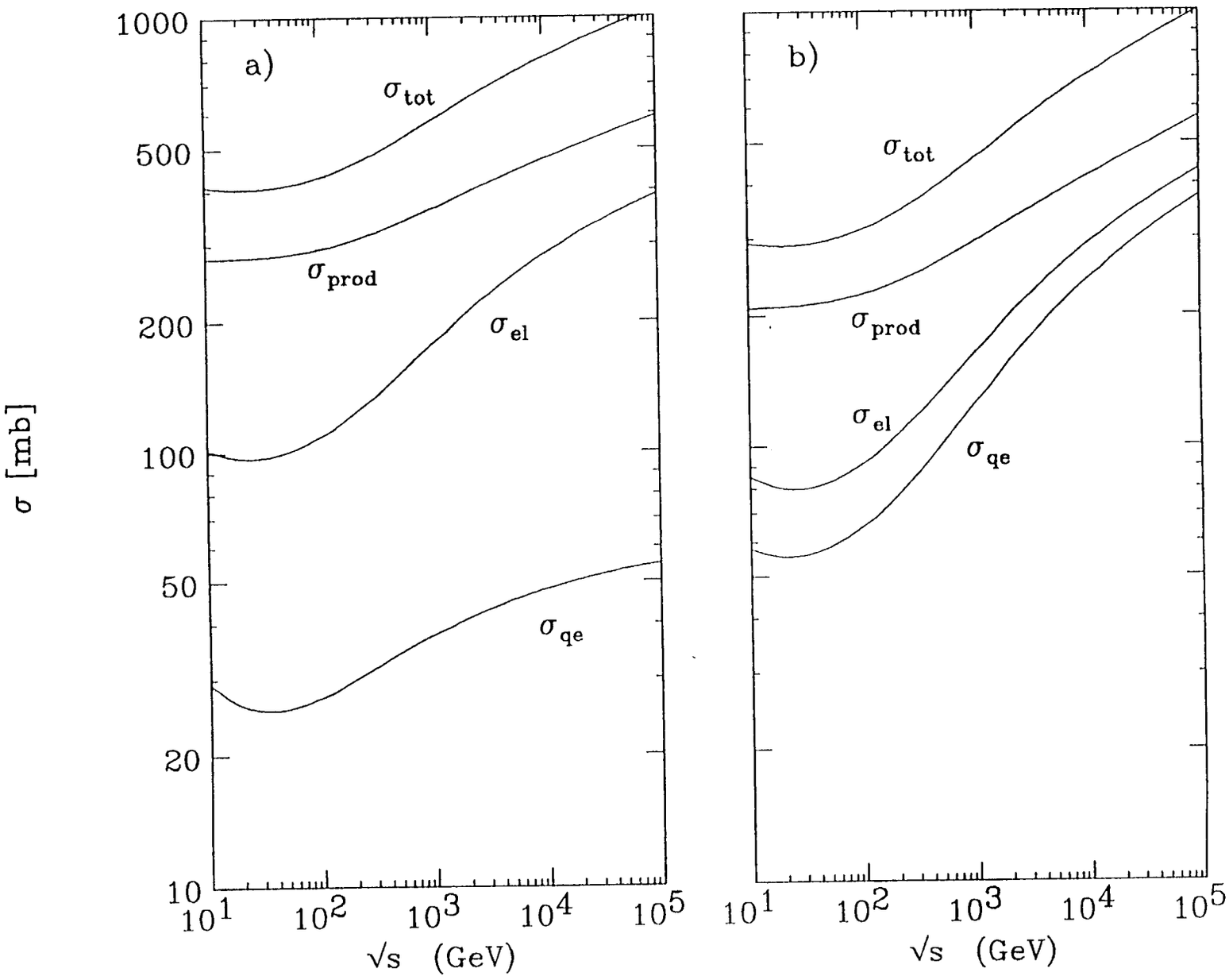
a)
b)
σ_{tot}
σ_{prod}
σ_{el}
σ_{qe}
σ [mb]
1000
500
200
100
50
20
10
10^1
10^2
10^3
10^4
10^5
√s (GeV)

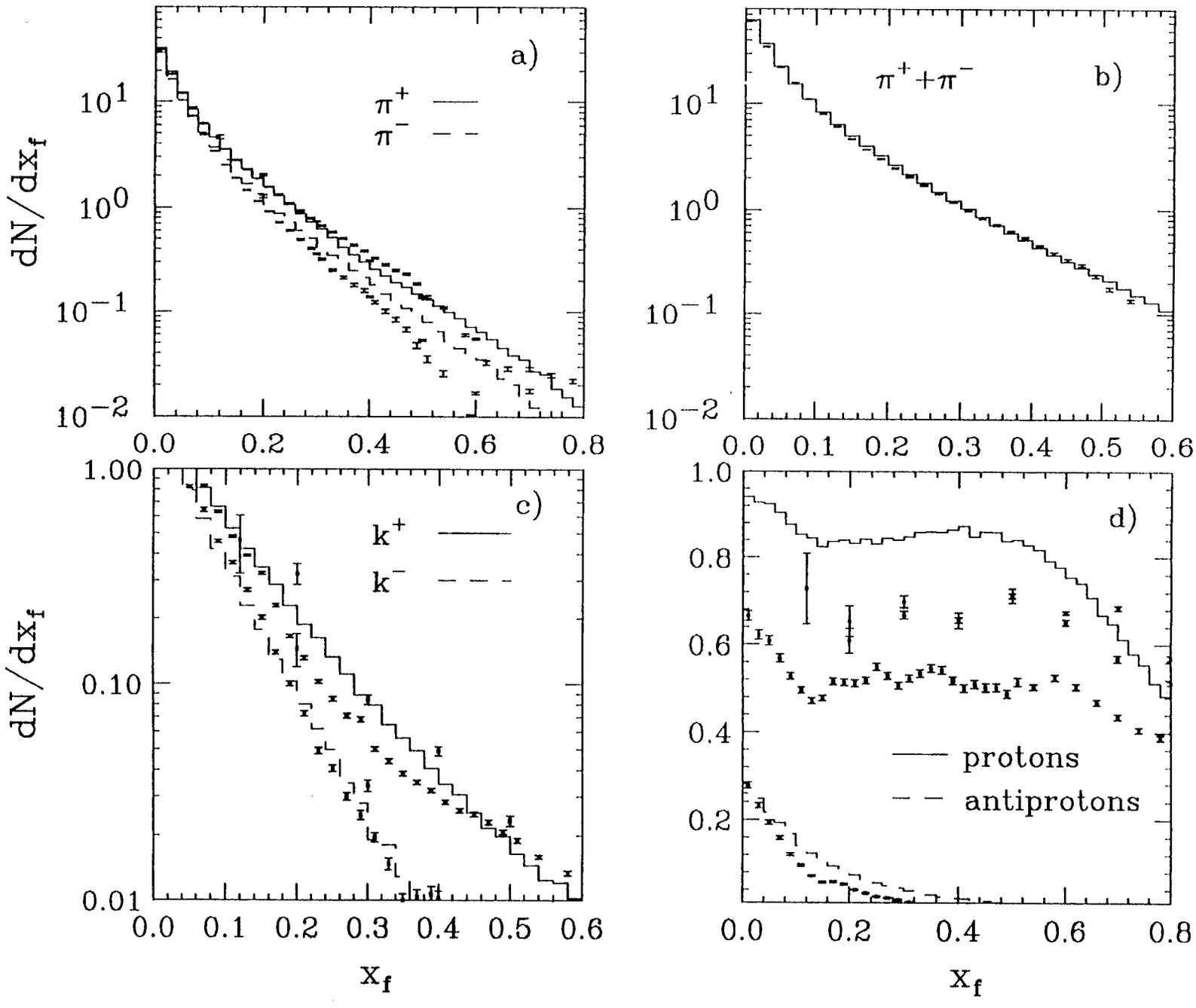
a)
π^+
π^-
10^1
10^0
10^{-1}
10^{-2}
0.0 0.2 0.4 0.6 0.8
b)
$\pi^+ + \pi^-$
10^1
10^0
10^{-1}
10^{-2}
0.0 0.1 0.2 0.3 0.4 0.5 0.6
c)
k^+
k^-
1.00
0.10
0.01
0.0 0.1 0.2 0.3 0.4 0.5 0.6
dN/dx_f
x_f
d)
protons
antiprotons
1.0
0.8
0.6
0.4
0.2
0.0 0.2 0.4 0.6 0.8
x_f

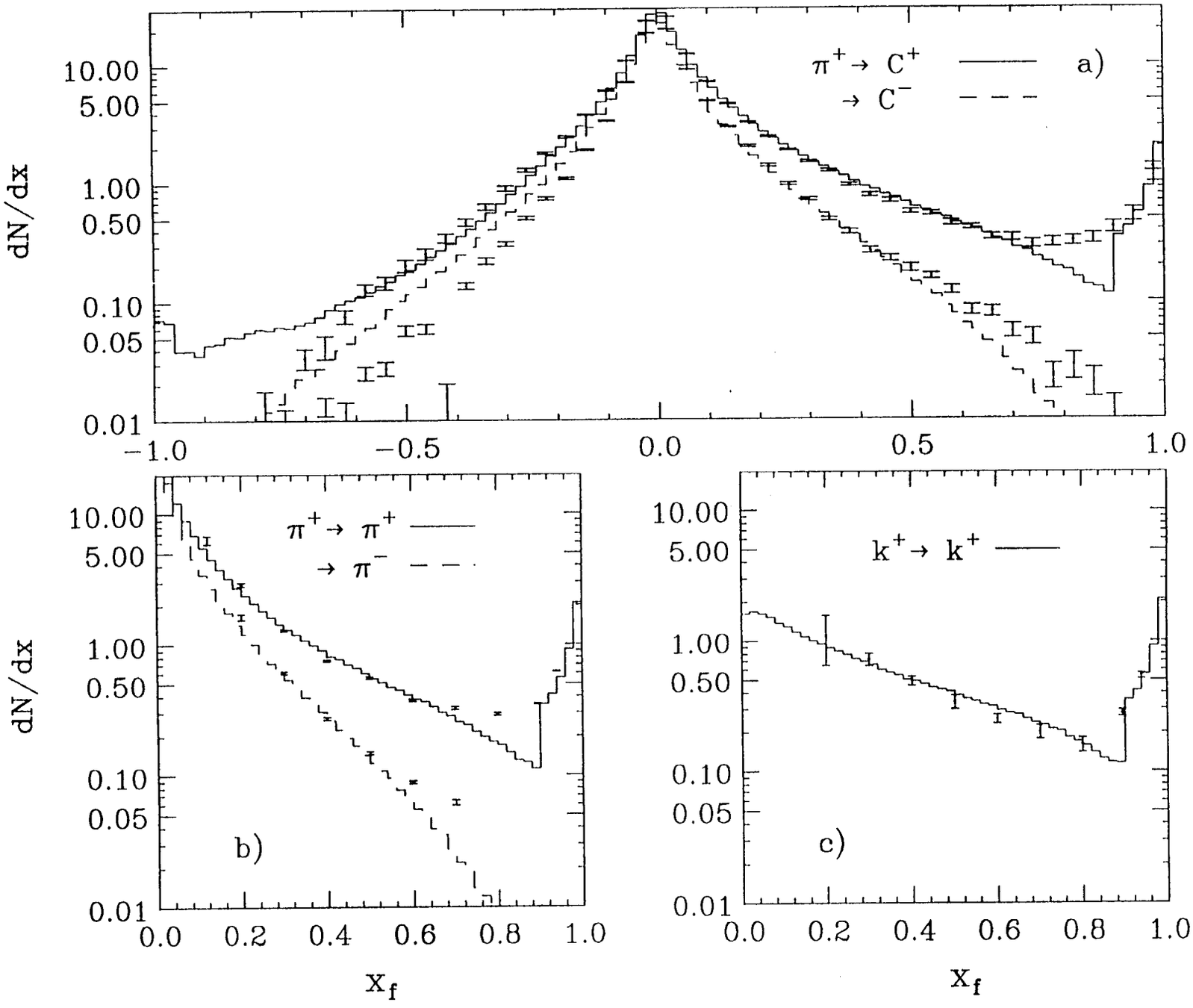
dN/dx
10.00
5.00
1.00
0.50
0.10
0.05
0.01
−1.0
−0.5
0.0
0.5
1.0
$\pi^+ \rightarrow C^+$
$\rightarrow C^-$
a)
$\pi^+ \rightarrow \pi^+$
$\rightarrow \pi^-$
b)
$k^+ \rightarrow k^+$
c)
0.0
0.2
0.4
0.6
0.8
1.0
x_f

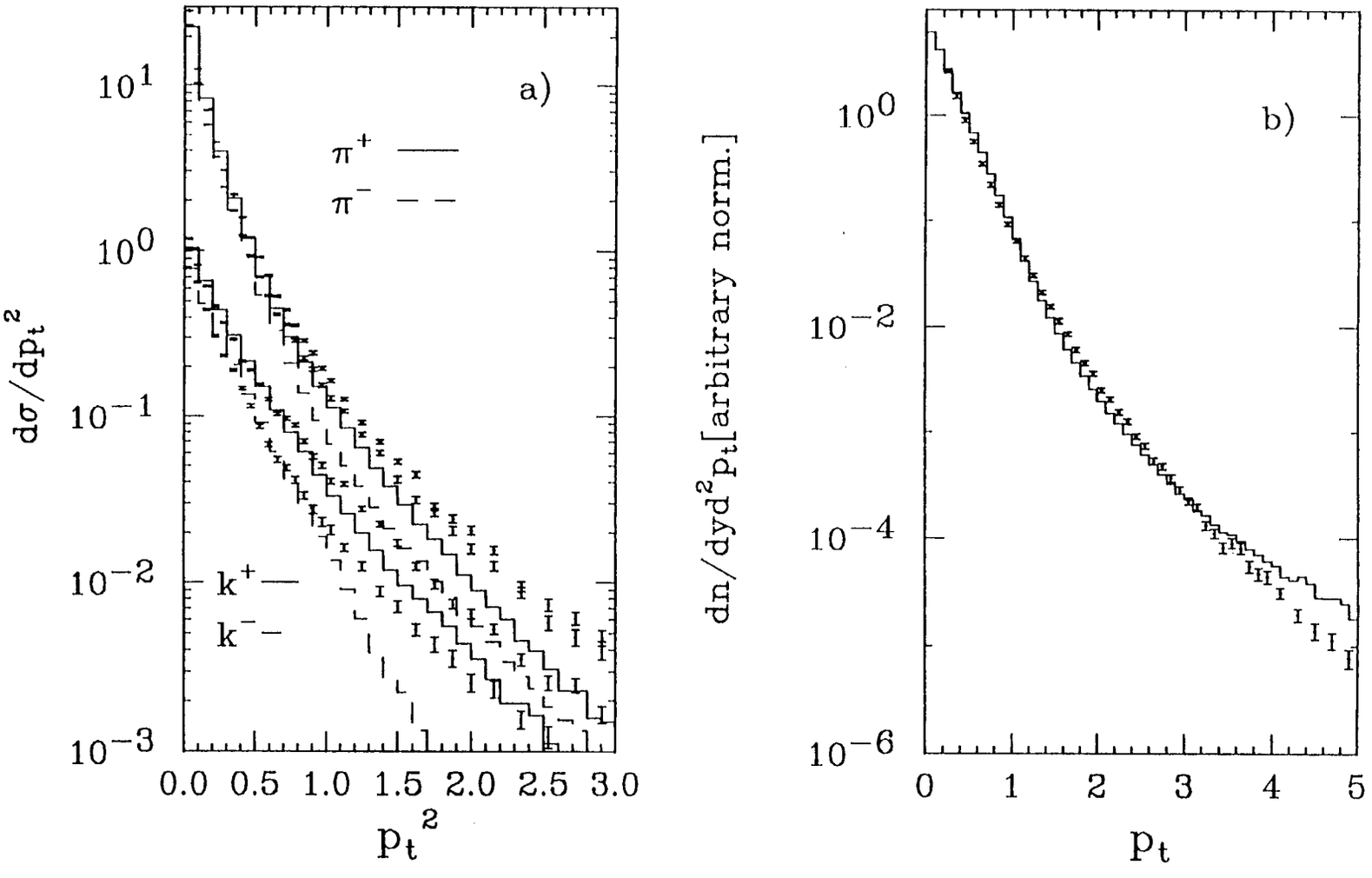
a)
π^+
π^-
k^+
k^-
$d\sigma/dp_t^2$
p_t^2
10^1
10^0
10^{-1}
10^{-2}
10^{-3}
0.0 0.5 1.0 1.5 2.0 2.5 3.0
b)
dn/dyd^2p_t[arbitrary norm.]
10^0
10^{-2}
10^{-4}
10^{-6}
0 1 2 3 4 5
p_t

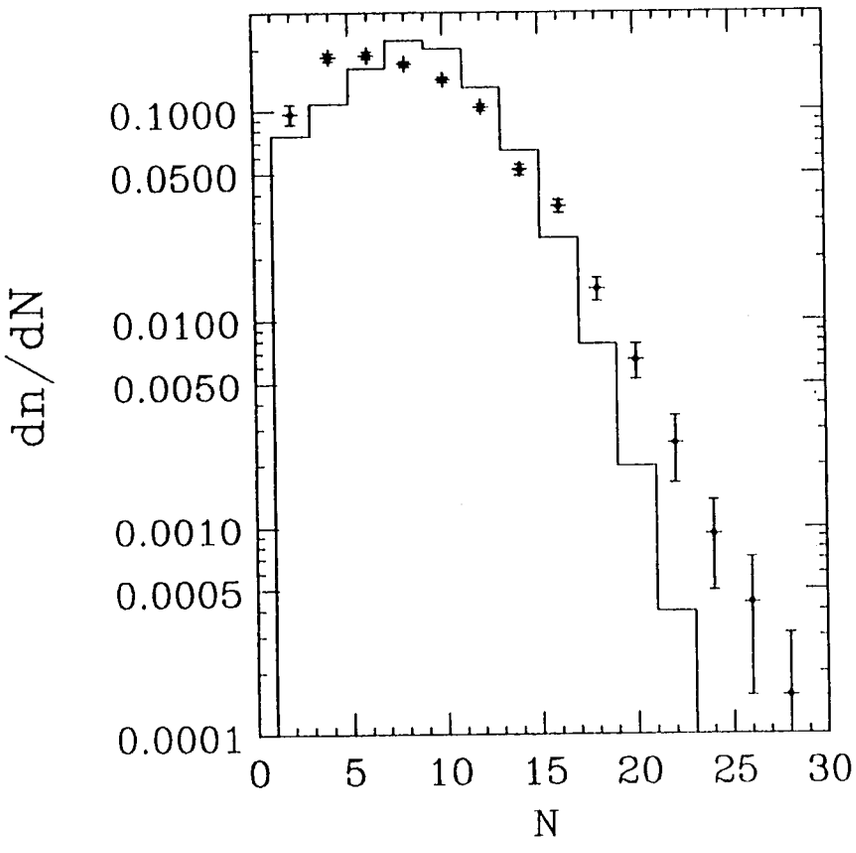
dn/dN
0.1000
0.0500
0.0100
0.0050
0.0010
0.0005
0.0001
0
5
10
15
20
25
30
N

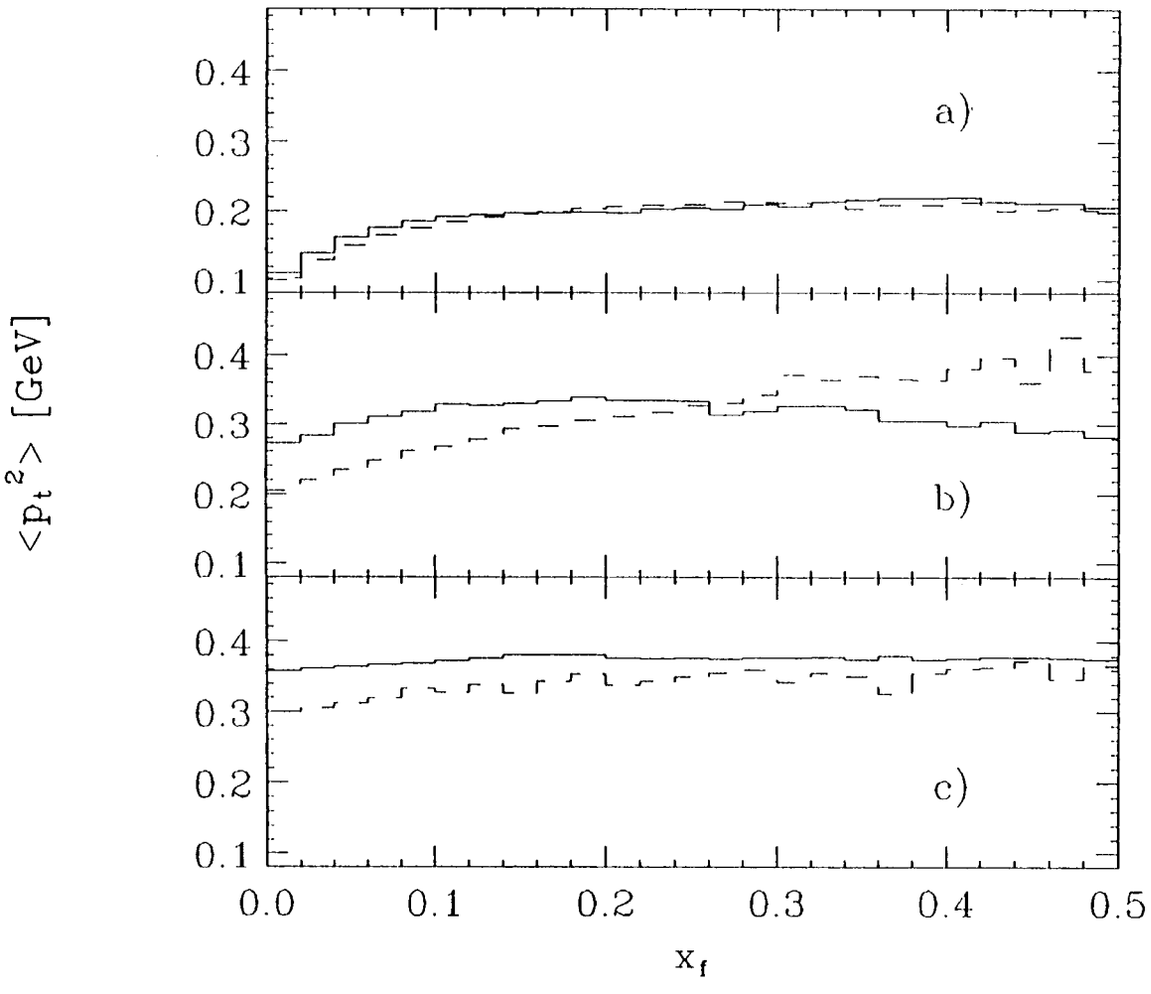
$\langle p_t^2 \rangle$ [GeV]
0.4
0.3
0.2
0.1
a)
b)
c)
0.0
0.1
0.2
0.3
0.4
0.5
x_f

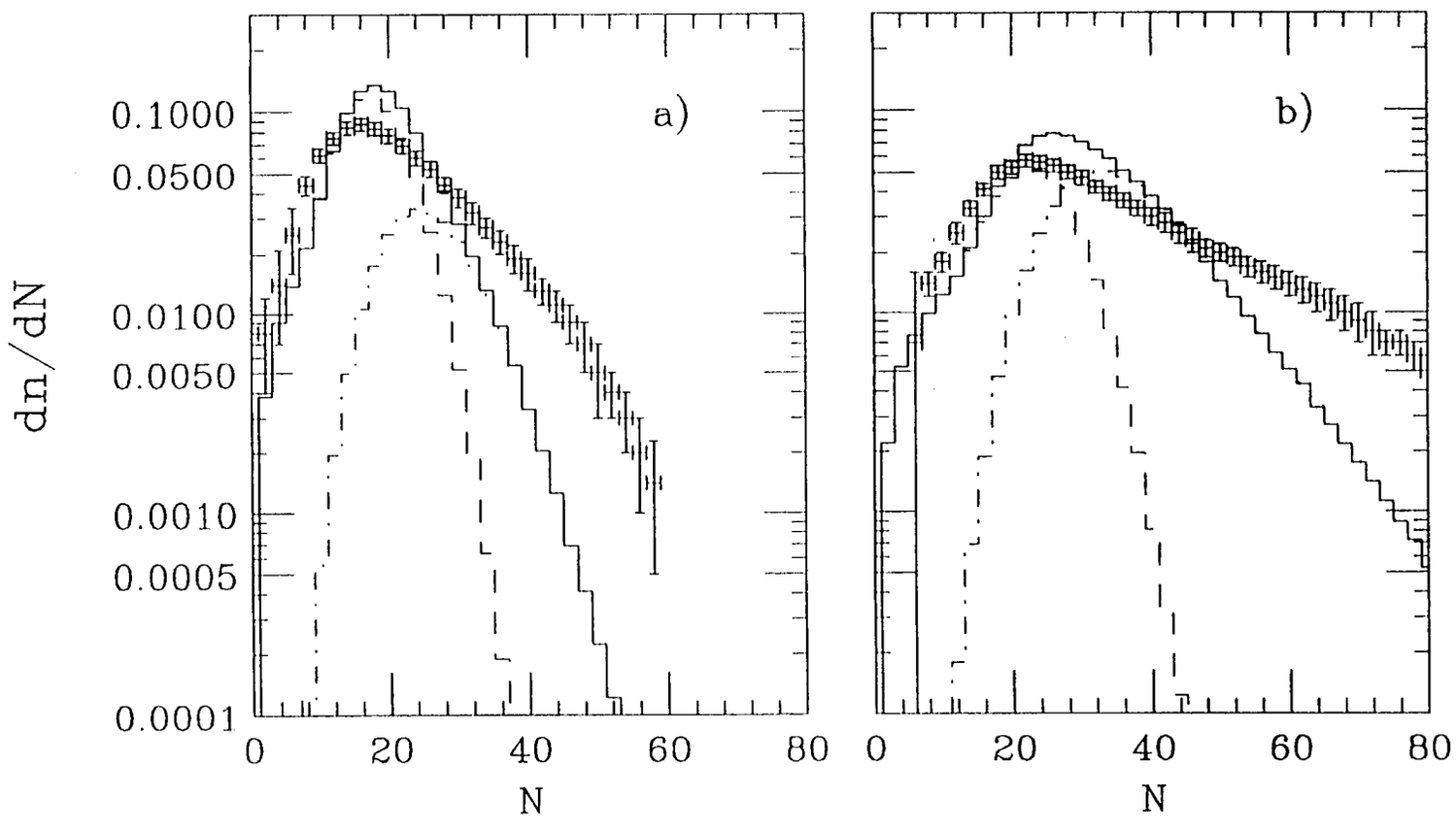
dn/dN
0.1000
0.0500
0.0100
0.0050
0.0010
0.0005
0.0001
a)
b)
0
20
40
60
80
N

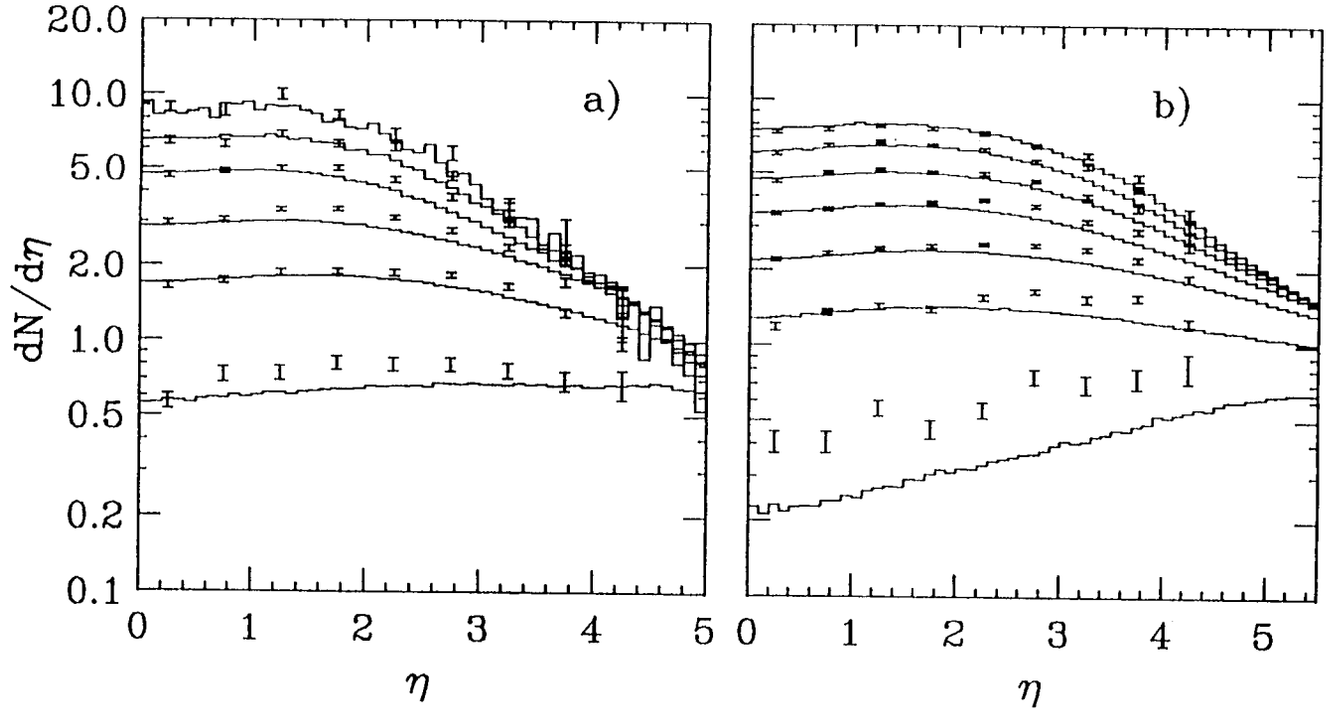
20.0
10.0
5.0
2.0
1.0
0.5
0.2
0.1
dN/dη
a)
b)
0
1
2
3
4
5
η
η

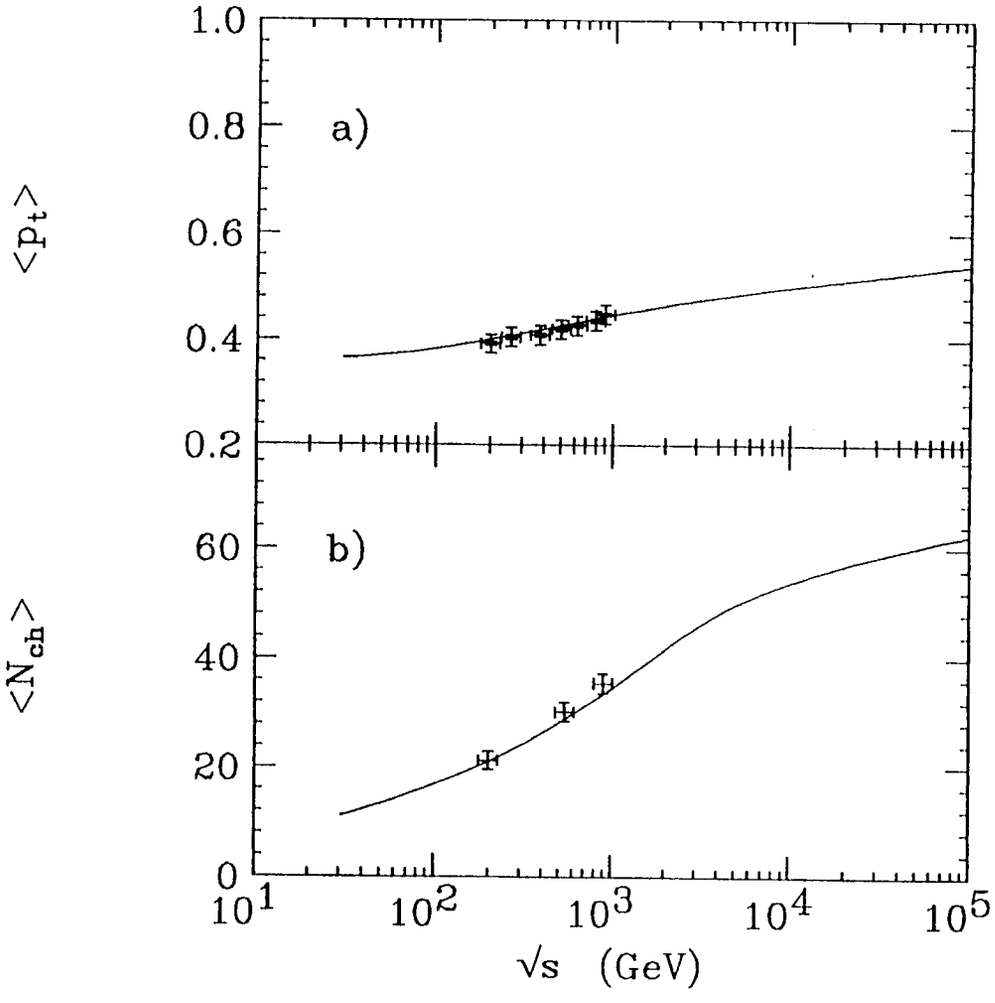
1.0
0.8
a)
0.6
0.4
0.2
60
b)
40
20
0
10^1
10^2
10^3
10^4
10^5
$\sqrt{s}$ (GeV)
$\langle p_t \rangle$
$\langle N_{ch} \rangle$

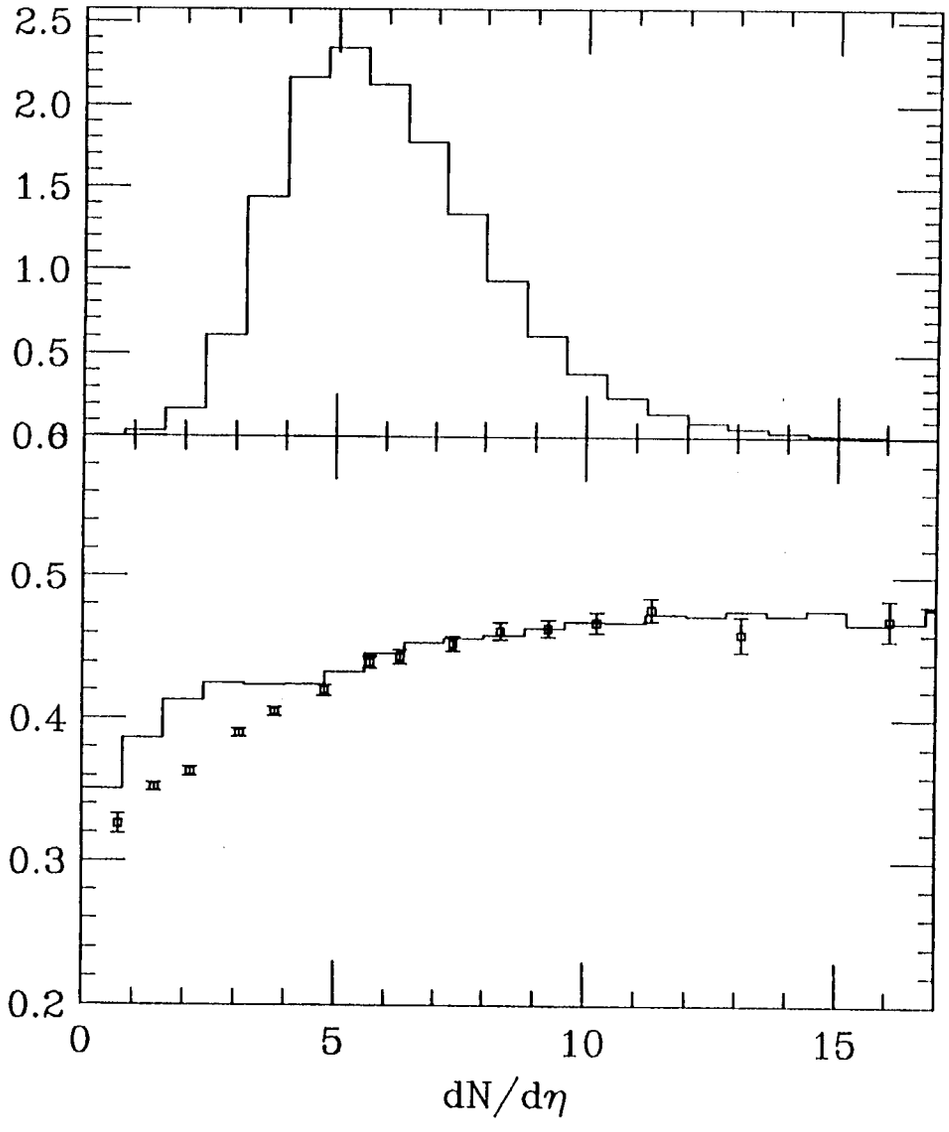
N
2.5
2.0
1.5
1.0
0.5
0.0
<p_t>
0.5
0.4
0.3
0.2
0
5
10
15
dN/dη

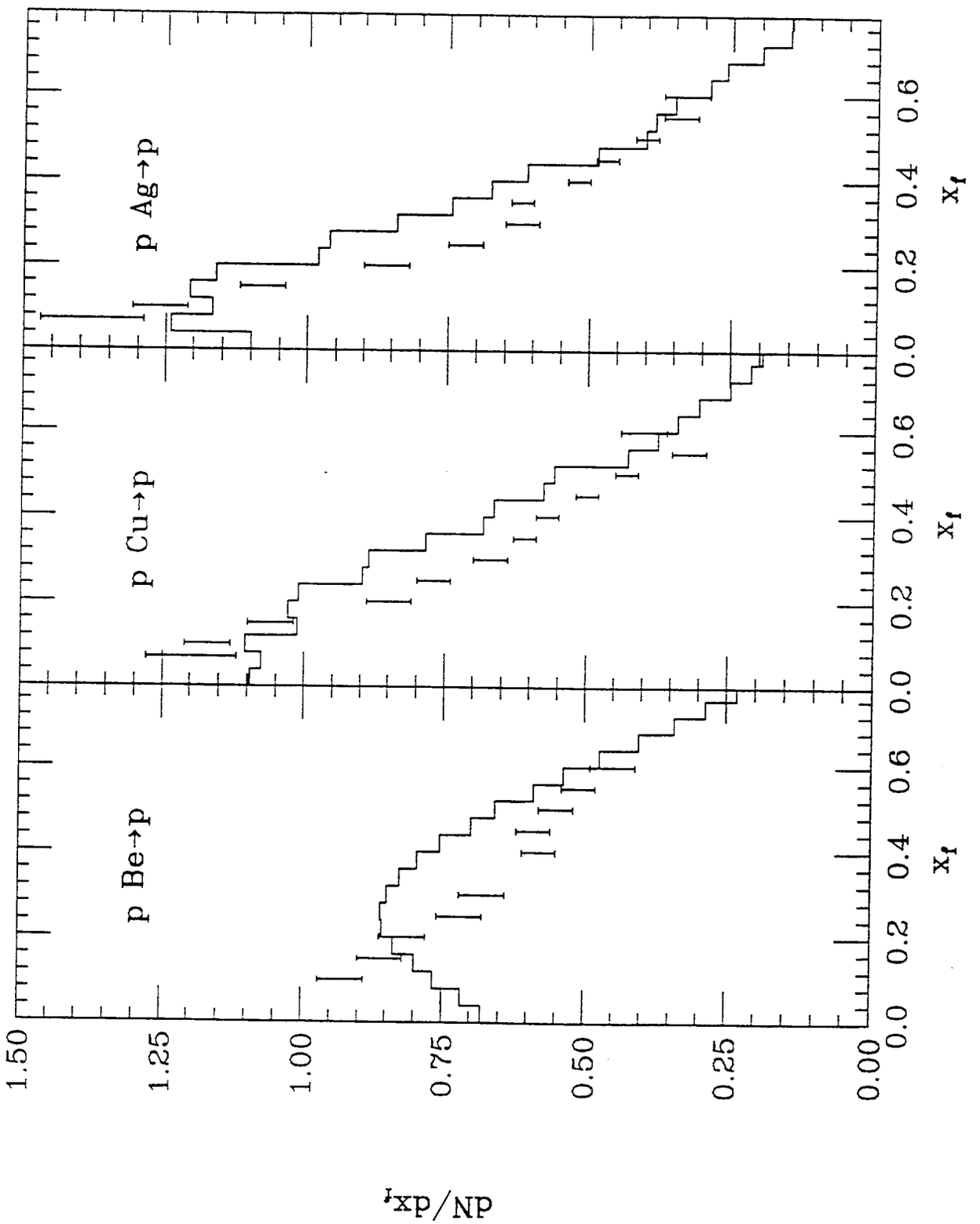
p Be→p
p Cu→p
p Ag→p
dN/dx_f
x_f
1.50
1.25
1.00
0.75
0.50
0.25
0.00
0.0
0.2
0.4
0.6
0.0
0.2
0.4
0.6
0.0
0.2
0.4
0.6

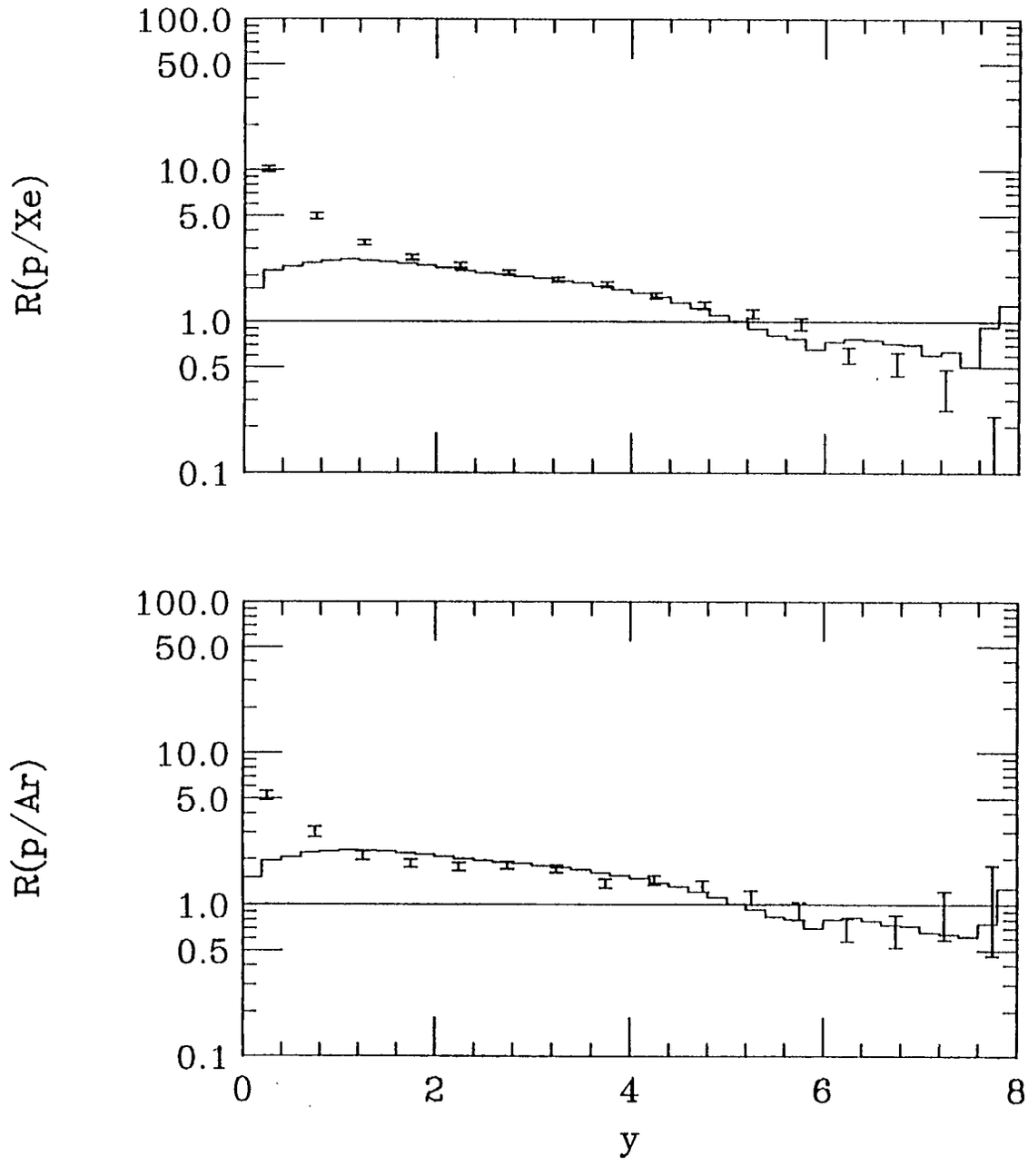
R(p/Xe)
100.0
50.0
10.0
5.0
1.0
0.5
0.1
R(p/Ar)
100.0
50.0
10.0
5.0
1.0
0.5
0.1
0
2
4
6
8
y

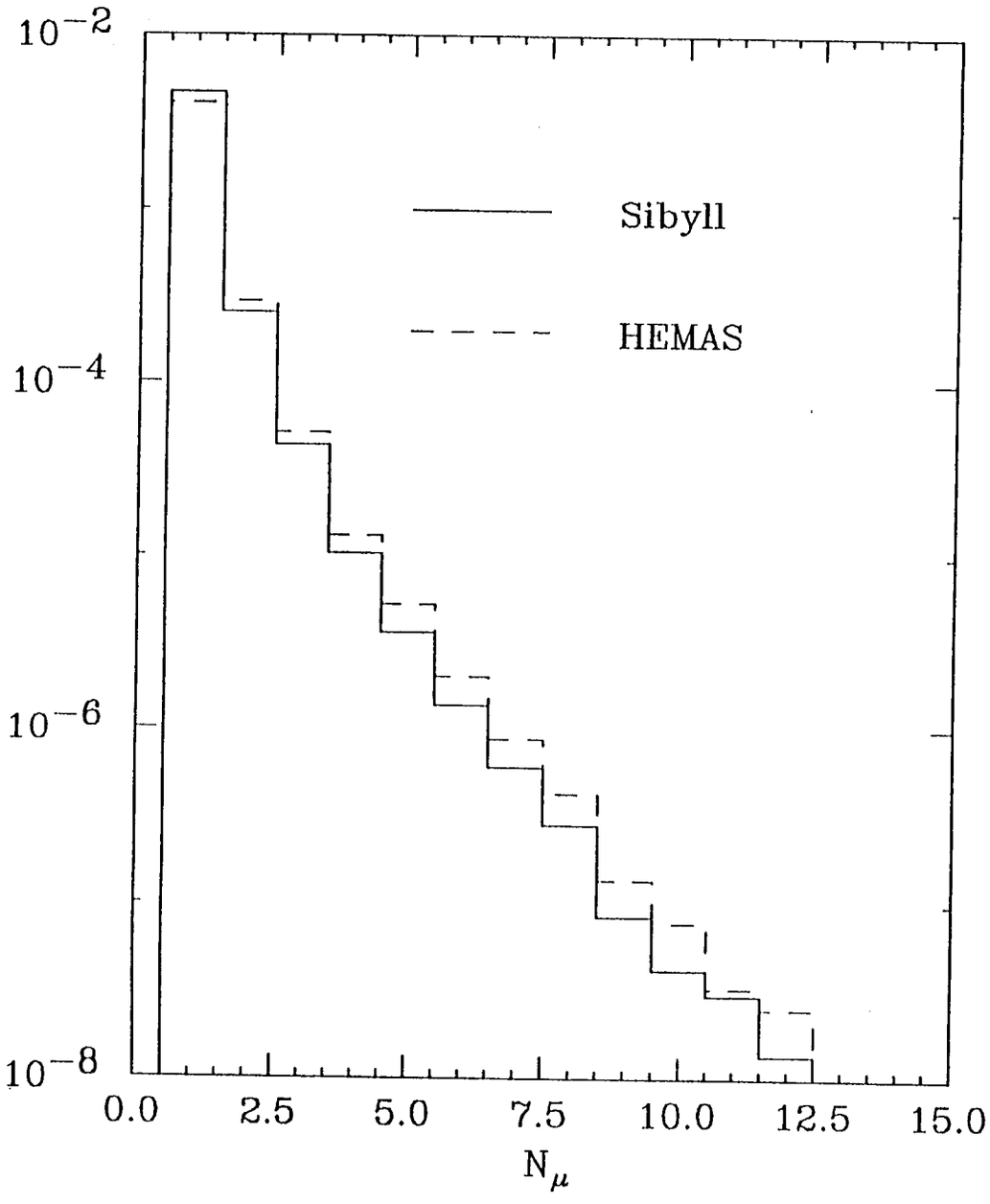
10^{-2}
10^{-4}
10^{-6}
10^{-8}
Sibyll
HEMAS
0.0
2.5
5.0
7.5
10.0
12.5
15.0
N_μ

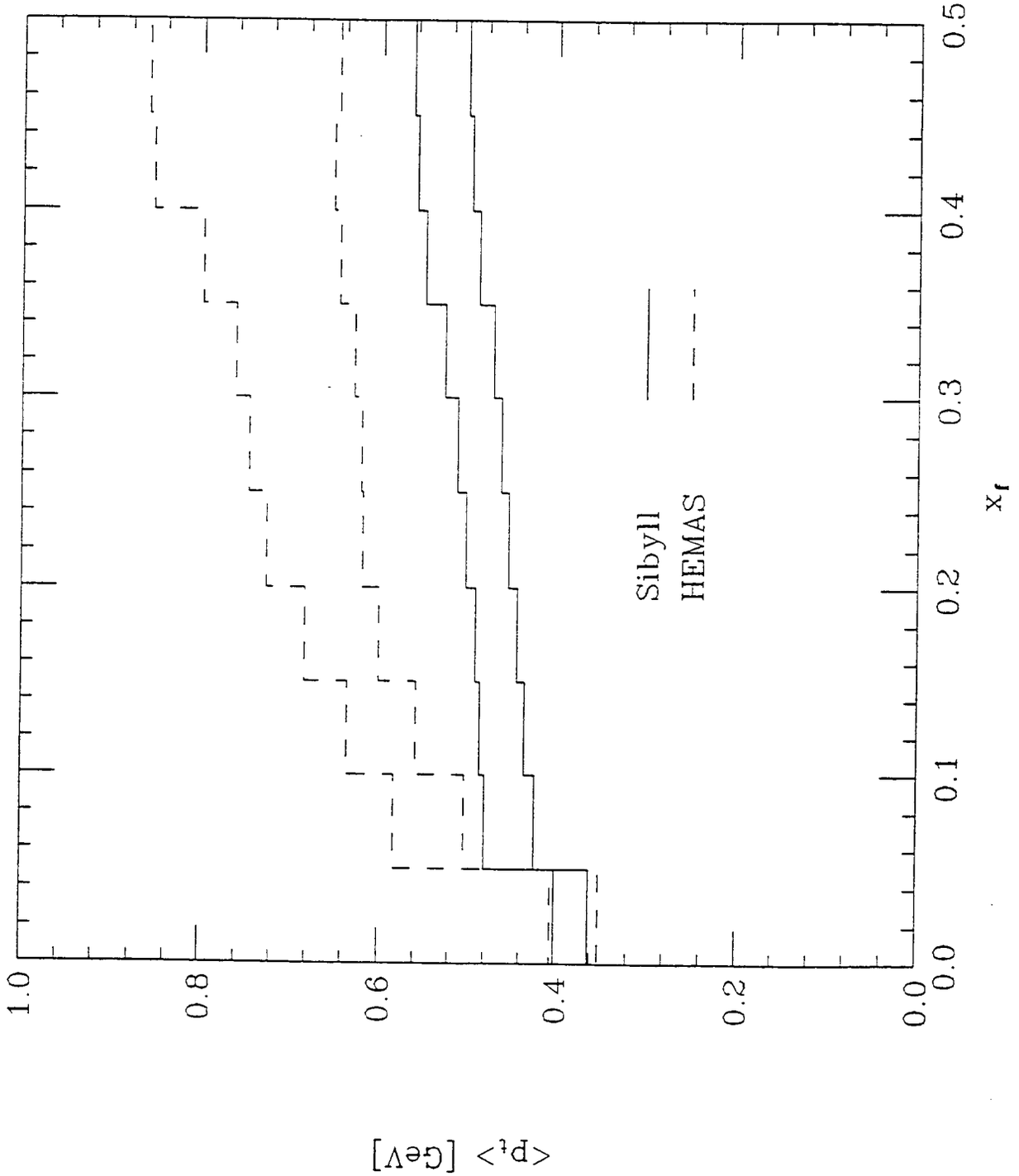
Sibyll
HEMAS
x_f
$\langle p_t \rangle$ [GeV]
0.0
0.1
0.2
0.3
0.4
0.5
0.0
0.2
0.4
0.6
0.8
1.0